



# Enhancing sulfacetamide degradation by peroxymonosulfate activation with N-doped graphene produced through delicately-controlled nitrogen functionalization via tweaking thermal annealing processes

Xiao Chen<sup>a,b</sup>, Wen-Da Oh<sup>c</sup>, Zhong-Ting Hu<sup>b</sup>, Yuan-Miao Sun<sup>d</sup>, Richard D. Webster<sup>e</sup>, Shu-Zhou Li<sup>d</sup>, Teik-Thye Lim<sup>a,b,\*</sup>

<sup>a</sup> Environmental Chemistry and Materials Centre, Nanyang Environment and Water Research Institute (NEWRI), Nanyang Technological University (NTU), 1 Cleantech Loop, CleanTech One, #06-08, Singapore 637141, Singapore

<sup>b</sup> School of Civil and Environmental Engineering, Nanyang Technological University, 50 Nanyang Avenue, Singapore 639798, Singapore

<sup>c</sup> Residues and Resource Reclamation Centre, Nanyang Environment and Water Research Institute (NEWRI), Nanyang Technological University, 1 Cleantech Loop, CleanTech One, Singapore 637141, Singapore

<sup>d</sup> School of Materials Science and Engineering, Nanyang Technological University, 50 Nanyang Avenue, 639798, Singapore

<sup>e</sup> Division of Chemistry and Biological Chemistry, School of Physical and Mathematical Sciences, Nanyang Technological University, 637371, Singapore

## ARTICLE INFO

### Keywords:

Nitrogen-doped graphene  
Sulfate radical  
Peroxymonosulfate  
Metal-free catalysis  
Sulfonamide antibiotics

## ABSTRACT

Nitrogen-doped graphenes (NG) fabricated through thermal annealing of graphene oxide (GO) and urea was applied to activate peroxymonosulfate (PMS) for sulfacetamide (SAM) degradation. The contents of reactive functional groups (graphitic N, pyridinic N, pyrrolic N, nitric oxide and C=O) and catalytic performance of NG were delicately controlled by adjusting thermal annealing temperature. Thermal annealing temperature of  $\geq 500^\circ\text{C}$  was required to produce the NG endowed with catalytic activity for SAM degradation via PMS activation. NG600 (NG prepared at  $600^\circ\text{C}$ ) with a high N doping level (16.0 wt%) and a most optimum amount of pyridinic N (38.4%N), pyrrolic N (31.8%N), graphitic N (25.9%N) and C=O groups (43.7%O) exhibited the most outstanding catalytic activity to activate PMS. NG600 with the controlled N bonding configurations possessed a higher SAM degradation efficiency than NGs prepared via other optimized synthesis methods. The specific surface area (SSA) contributed less significantly than N doping to the SAM degradation performance. Increments in the PMS dosage and catalyst loading were both conducive to the catalytic performance of NG. The presence of  $\text{NO}_3^-$  in the NG600/PMS system had a negligible influence on SAM degradation but  $\text{Cl}^-$  and humic acid decreased the SAM degradation rate. Experiments using chemical scavengers and electron paramagnetic resonance (EPR) study revealed that SAM degradation process follows predominantly the radical pathway with sulfate radical ( $\text{SO}_4^{\cdot-}$ ) as the main reactive oxygen species over the non-radical pathway. Density functional theory (DFT) calculations suggest that graphitic N can facilitate PMS adsorption on the NG and SAM degradation. This study improves the understanding on the role of different surface N functional groups of NG in the PMS activation.

## 1. Introduction

The occurrence, fate and potential risks of antibiotics in the environment have become a worldwide concern in recent years [1,2]. Being commonly used as human and veterinary medicines for treating and preventing infections [3], sulfonamide antibiotics can enter the environment as partially unmetabolised form or biotransformed product from human body and animal organisms, or as the used drugs discharged into sewage [4]. A widespread distribution of sulfonamides

in the aquatic environment can induce the evolution of antibiotic resistant pathogenic bacteria, posing a threat to the ecosystem and human health even at a low concentration [5,6].

Compared with conventional treatment processes (e.g., flocculation [7], membrane filtration [8], ozonation [9] and biological treatment [10]) and advanced oxidation processes (AOPs) involving hydroxyl radical ( $\text{HO}\cdot$ ) (e.g.,  $\text{UV}/\text{H}_2\text{O}_2$ ,  $\text{O}_3/\text{H}_2\text{O}_2$  or Fenton) [7] reported for sulfonamides removal, sulfate radical-based advanced oxidation process (SR-AOP) has the following merits: (1) a higher redox potential of

\* Corresponding author at: Environmental Chemistry and Materials Centre, Nanyang Environment and Water Research Institute (NEWRI), Nanyang Technological University (NTU), 1 Cleantech Loop, CleanTech One, #06-08, Singapore 637141, Singapore.

E-mail address: [CTTLIM@ntu.edu.sg](mailto:CTTLIM@ntu.edu.sg) (T.-T. Lim).

<https://doi.org/10.1016/j.apcatb.2017.11.071>

Received 18 August 2017; Received in revised form 30 October 2017; Accepted 27 November 2017

Available online 27 November 2017

0926-3373/ © 2017 Elsevier B.V. All rights reserved.

sulfate radical ( $\text{SO}_4^{\cdot-}$ ) ( $E^\circ = 2.5\text{--}3.1\text{ V}$ ) than that of  $\text{HO}^\cdot$  ( $E^\circ = 2.8\text{ V}$ ), (2) a longer half-life of  $\text{SO}_4^{\cdot-}$  (30–40  $\mu\text{s}$ ) relative to its selectivity, (3) a wider range of pH tolerance and (4) the slow utilization of precursor oxidants [11,12]. Thus, SR-AOP is an effective alternative to degrade persistent organic pollutants.  $\text{SO}_4^{\cdot-}$  as a strong oxidant can be produced by activation of peroxymonosulfate (PMS) or persulfate (PS) via scission of the peroxide O–O bond [13]. Previously, heat/transition metal (e.g.,  $\text{Co}^{2+}$ )/UV activated PS/PMS have been studied for the complete degradation of sulfonamides [14]. However, the metal activated PMS process (e.g.,  $\text{Co}_3\text{O}_4$ /PMS,  $\text{Co}^{2+}$ /PMS) has problems of toxic transition metal leaching and difficulty in separating and recovering homogeneous metal catalysts [15]. The energy-based PMS activation process (e.g., UV/PMS, ultrasound/PMS or heat/PMS) needs a constant external energy supply [16].

By contrast, carbocatalysts as an alternative can be used as a metal-free material for PMS activation. Nanocarbon allotropes were used in different molecular dimensions. 0D fullerene and nanodiamonds, 1D single-walled carbon nanotubes (SWCNTs) and multi-walled carbon nanotubes (MWCNTs), 2D graphene and graphitic carbon nitride (g-C<sub>3</sub>N<sub>4</sub>), and 3D hexagonally ordered mesoporous carbon (CMK-3) and cubically-ordered mesoporous carbon (CMK-8) were developed for catalytic oxidation of phenol via PMS activation [17]. Graphene has attracted widespread scientific interests for the last decade due to its fascinating properties, such as the large specific surface area (SSA), high electrical conductivity and mobility of charge carriers, and structural and surface tunability, which has opened a new application perspective for the 2D materials. The doping of heteroatom (e.g., N, B, S, or P) into graphene carbon lattice can effectively tailor the properties of pristine graphene. N doping has been proposed as the most promising one due to (1) the production of modified functional groups and more defective sites, (2) the enhanced electron mobility resulting from activated  $\pi$ -electrons in  $\text{sp}^2$  carbon via  $\text{sp}^2$  conjugation, and (3) the modification of electron density of the local carbon atom neighboring the N dopants [18,19]. Therefore, nitrogen-doped graphene (NG) as a PMS activator was investigated for sulfonamides degradation in this study.

The four major N bonding configurations in N-doped carbocatalysts are pyridinic N, pyrrolic N, quaternary N (or graphitic N) and nitric oxide. Pyridinic N with  $\text{sp}^2$  hybridization exists in a six-membered ring bonding with two C atoms at the edges of graphene, donating one p electron to the  $\pi$ -system. Pyrrolic N with  $\text{sp}^2$  hybridization can exist in a five-membered ring to donate two p electrons to the aromatic system. Graphitic N refers to  $\text{sp}^2$  hybridized N atom bonding with three  $\text{sp}^2$  C atoms. Nitric oxide refers to N atoms bonding with one O atom and two C atoms. The Lewis basic sites with lone-pair electrons, such as pyridinic N, pyrrolic N and ketonic groups, possess a remarkable potential for the redox process, which is conducive to the radical production via PMS activation. Pyridinic N can efficaciously modify the valence band structure of graphene by increasing the density of  $\pi$  states near the Fermi level and reducing the work function [20]. The abundant free-flowing  $\pi$ -electrons from  $\text{sp}^2$  carbons of graphene can be activated through conjugating with the lone-pair electrons of N dopants to induce PMS activation and production of free radicals [21]. Graphitic N with a higher electronegativity than C atoms can cause electron transfer from the adjacent C atoms to the N atom, breaking the inertness of  $\text{sp}^2$  bonded carbon network and leading to positively charged neighboring C atoms and negatively charged N atoms as active sites to activate PMS via non-radical pathway [22]. Graphitic N possesses the highest thermal stability, whereas pyrrolic N has the lowest thermal tolerance [23]. Thus, the synthesis temperature plays a crucial role in the N doping content and configuration in carbon allotropes [24]. Besides, N sources and synthesis conditions (ambient or inert) can also affect N bonding configurations. In previous studies, the influence of synthesis temperature has been explored on the NG fabricated with nitrogen sources different from urea, such as melamine [25] and ammonium nitrate [26], or on other types of catalysts, such as nitrogen-doped carbon nanotube (NCNT) [27] and CuO [28] for pollutant degradation

via PS/PMS activation. Compared with melamine and ammonium nitrate, urea can act as a better N source to endow as-prepared the NG with a high N doping level and a better reducibility without polycondensation, leading to a higher catalytic ability for PMS activation [29].

As such, we formulate our hypothesis: (1) the concentration of reactive N functional groups can be tuned through the controlled synthesis temperature and choice of N source, and (2) different N functional groups will therefore endow different NGs with different performances in terms of catalytic efficiency, pollutant degradation mechanism, and catalyst reusability. To the best of our knowledge, limited studies have been conducted about the effect of thermal annealing temperature on N bonding configurations of NG synthesized with urea as a nitrogen source and the catalytic performance of the as-prepared NG for pollutant degradation via PMS activation.

Therefore, the objectives of this research are as follows: (1) to develop NGs with different N doping levels and N bonding configurations using urea as a nitrogen source through the controlled thermal annealing temperature (400, 500, 600, 700 and 800°C), investigate the variation of their intrinsic properties (e.g., N doping level, N bonding configuration) and extrinsic properties (e.g., SSA) with the thermal annealing temperature, and probe their catalytic performances for sulfacetamide (SAM) degradation via PMS activation. The SAM is one of the most commonly used sulfonamides and frequently detected in water and soil [30]; (2) to compare the NG endowed with the most optimum N bonding configurations in this research with NGs prepared via other optimized synthesis methods found in the literature, and probe the relationship between their properties and their catalytic performances for SAM degradation via PMS activation.

## 2. Experimental

### 2.1. Chemicals

All the chemicals were of analytical grade (AR) and used without further purification. Natural graphite powder with 325 mesh (> 99.9%), hydrogen peroxide (35%w/w), Oxone ( $2\text{KHSO}_5 \cdot \text{KHSO}_4 \cdot \text{K}_2\text{SO}_4$ ) were obtained from Alfa Aesar, concentrated sulfuric acid (98%), potassium permanganate (99%), sodium nitrate (99%), hydrochloric acid (37%), urea (99.0–100.5%), melamine ( $\geq 99\%$ ), ammonium nitrate ( $\geq 98\%$ ), sulfacetamide (SAM) ( $\geq 98\%$ ), sulfanilamide (SNM) ( $\geq 98\%$ ), sulfamethoxazole (SMX) ( $\geq 98\%$ ), and sulfathiazole (STZ) ( $\geq 98\%$ ), phenol ( $\geq 99\%$ ), sodium perchlorate ( $\geq 98\%$ ), nitrobenzene ( $\geq 99\%$ ), sodium nitrate ( $\geq 98\%$ ), humic acid and 5,5-dimethylpyrrolidine-oxide (DMPO) were obtained from Sigma-Aldrich, absolute ethanol (99.9%, Fisher chemical), methanol (HPLC grade, VWR), sodium hydroxide (pellet, Schedelco), sodium chloride (99.5–100.5%, Merck) were used in this study. Milli-Q ultrapure water (18.2 M $\Omega$  cm at 25°C) was used for all the experiments.

### 2.2. NG synthesis

Graphene oxide (GO) was prepared via the modified Hummers' method [31] (Text S1). Exactly 200 mg of GO was dispersed in 100 mL water in a 250-mL beaker and sonicated for 30 min, followed by adding 1 g urea and the mixture was stirred at 500 rpm for 30 min for urea dissolution. Then the temperature of the mixture was increased to 55°C while stirring using a hotplate to evaporate water. The resulted dried GO/urea mixture was grinded and calcined at 400, 500, 600, 700 and 800°C in a N<sub>2</sub> atmosphere for 30 min in the tubular furnace with the ramping rate of 5°C min<sup>−1</sup>, respectively. The final products were grinded, filtered and washed by a large amount of water and absolute ethanol in sequence and then dried at 60°C overnight in a vacuum oven. The N-doped products were denoted as NG400, NG500, NG600, NG700 and NG800, respectively. Reduced graphene oxide (RGO) was produced by the same procedure but without adding urea and calcined at 600°C

in a  $N_2$  atmosphere. The resulted product was denoted as RGO600. For comparison, NG was also prepared via other optimized synthesis methods found in the literature (NG-melamine- $N_2$  via thermal annealing method [25], NG-urea-HT via hydrothermal method [32] and NG- $NH_4NO_3$ -air via low temperature combustion methods [21]) (Text S1).

### 2.3. Characterization

The crystal structure was investigated by X-ray diffraction (XRD, Bruker D8 Advance) with Cu-K $\alpha$  ( $\lambda = 1.5418 \text{ \AA}$ ) operated at 40 kV and 40 mA in a  $2\theta$  range of  $5\text{--}80^\circ$  with a scan rate of  $0.02^\circ \text{ s}^{-1}$ . The morphology and structure analysis were conducted on field emission scanning electron microscopy (FESEM, JEOL JSM-7600F) and transmission electron microscopy (TEM, JEOL JEM-2010). Energy-dispersive X-ray (EDX) maps were taken on the FESEM with an EDX spectrometer. The thermogravimetric analysis (TGA) was performed by the thermogravimetric analyzer (PerkinElmer, TGA-4000) with a heating rate of  $10^\circ \text{C min}^{-1}$  under air atmosphere. The Brunauer-Emmett-Teller (BET) model and Barrett-Joyner-Halenda (BJH) method relating to the  $N_2$  adsorption-desorption isotherm were used to analyze the SSA and the pore size distribution, respectively, on Quantachrome Autosorb-1 analyzer (77 K). Fourier transform infra-red spectra (FTIR) were recorded on a PerkinElmer GX FTIR system. X-ray photoelectron spectroscopy (XPS) studies were carried out using a Kratos Axis Supra spectrophotometer with a dual anode monochromatic K $\alpha$  excitation source. All binding energies for carbon, nitrogen and oxygen elements were corrected against an adventitious carbon C1s core level at 284.8 eV. All XPS peaks were fitted using Shirley background together with Gaussian-Lorentzian function using CASA XPS software. The elemental composition was analyzed on a PerkinElmer Series II 2400 CHNS/O analyzer. Total organic carbon (TOC) analysis was conducted on a Shimadzu TOC-vcph analyzer. Raman spectra were collected on a LabRAM ARAMIS Horiba Jobin Yvon instrument with a 532-nm wavelength laser. PMS concentration was determined by iodometric method [33]. Specifically, 5 mL sample was mixed with 1 g KI and then capped and aged for 30 min after vigorously shaking. The concentration of  $I_3^-$  formed which has a strong positive correlation with PMS concentration can be measured with UV-vis spectrometer at  $\lambda_{\text{max}} = 352 \text{ nm}$ . The Electron paramagnetic resonance (EPR) study was conducted using a Bruker Biospin ELEXSYS II E500 EPR spectrometer in continuous wave X-band mode. The modulation amplitude was 0.5 G and microwave power was 0.2 mW. The reactive radicals ( $SO_4^{\cdot -}$  and  $HO^{\cdot}$ ) generated from PMS activation were captured by a spin trapping agent 5,5-dimethylpyrroline-oxide (DMPO). The EPR spectra were analyzed by the spin-fitting package of Bruker Xeon software. The simulated spectrum was based on hyperfine coupling constants of  $\alpha N = 7.23 \text{ G}$ ,  $\alpha H^\beta = \alpha H^{\gamma 1} = 4.00 \text{ G}$ .

### 2.4. Adsorption and catalysis evaluation

The catalytic performance of NG via PMS activation was evaluated through SAM degradation. The reaction took place in a 100-mL beaker with 50 mL SAM solution ( $10 \text{ mg L}^{-1}$ ), catalyst loading ( $0.2 \text{ g L}^{-1}$ ) and PMS dosage ( $0.5 \text{ mM}$  PMS, which is commercially available as Oxone) and pH in the NG/PMS system was adjusted to 7 with 1 M NaOH. 0.5 mL of the aliquot was withdrawn at the designated time intervals and filtered through  $0.45 \mu\text{m}$  membrane and injected into a vial, followed by adding 0.5 mL methanol as a quenching agent. Then the SAM concentration was measured by high-performance liquid chromatography (HPLC, PerkinElmer) with mobile phase of 60% methanol: 40% deionized water at a flow rate of  $0.6 \text{ mL min}^{-1}$  in an isocratic condition. Reverse phase column (Hypersil Gold,  $150 \text{ mm} \times 4.6 \text{ mm} \times 5 \mu\text{m}$ ) was employed. UV detector was used at  $\lambda_{\text{max}} = 256 \text{ nm}$ . The adsorption experiment was conducted following the same procedure as catalytic evaluation without adding PMS. Both

the residual PMS and TOC were measured within 60 min. The effect of catalyst loading ( $[\text{catalyst}] = 0.1, 0.2 \text{ and } 0.3 \text{ g L}^{-1}$ ,  $[\text{PMS}] = 0.5 \text{ mM}$ ,  $[\text{SAM}] = 10 \text{ mg L}^{-1}$ ,  $\text{pH} = 7$ ), PMS dosage ( $[\text{PMS}] = 0.2, 0.5 \text{ and } 0.9 \text{ mM}$ ,  $[\text{catalyst}] = 0.2 \text{ g L}^{-1}$ ,  $[\text{SAM}] = 10 \text{ mg L}^{-1}$ ,  $\text{pH} = 7$ ) and common matrix species ( $[\text{Cl}^-] = 100 \text{ mg L}^{-1}$ ,  $[\text{NO}_3^-] = 10 \text{ mg L}^{-1}$ ,  $[\text{humic acid}] = 5 \text{ mg L}^{-1}$ ,  $[\text{catalyst}] = 0.2 \text{ g L}^{-1}$ ,  $[\text{PMS}] = 0.5 \text{ mM}$ ,  $[\text{SAM}] = 10 \text{ mg L}^{-1}$ ,  $\text{pH} = 7$ ) on the catalytic degradation in the NG/PMS system was investigated. Phenol, nitrobenzene and  $\text{NaClO}_4$  were selected as quenching agents for possible radical and non-radical pathways in NG/PMS system to investigate the possible SAM degradation mechanism in the NG/PMS system. The major SAM intermediates produced in the NG600/PMS system were investigated using the LCMSMS system (Agilent 6460 Triple Quad LC/MS). All the catalyst experiments were performed in triplicate. The results showed that the relative errors were less than  $\pm 5\%$ .

### 2.5. Reusability

After adsorption and degradation of SAM in the NG/PMS system, the catalyst was collected by vacuum filtration using  $0.45 \mu\text{m}$  membrane and washed by methanol and water to neutral pH, and then re-dispersed in the fresh SAM solution. After three consecutive cycles, the catalyst was collected, washed and dried in the freeze dryer for further characterization.

### 2.6. Computational methods

The density functional theory (DFT) calculations were performed by using Gaussian 09 program package. The rB3LYP functional was used to describe the exchange-correlation effects. All calculations were carried out with the 6–31G\* basis sets. In the simulation, nonperiodic graphene cluster was employed and graphitic N was created by replacing one C atom in the graphene, consistent with the model proposed by Duan et al. [34]. The convergence tolerance of  $10^{-6}$  Hartree (1 hartree = 27.21 eV) energy change was applied in all cases.

## 3. Results and discussion

### 3.1. Characteristics of carbon materials

#### 3.1.1. NGs prepared at different temperatures

Fig. 1 shows the FESEM images of GO, RGO600 and NG600, indicating that the thermal annealing process increases the folding and exfoliation of GO (which has a smooth and wave-like structure). By contrast, NG600 was found to be more exfoliated and crumpled at the edge of the doped graphitic sheets probably derived from the defective sites caused by N doping. The TEM images reveal that NG600 still maintained the characteristic two-dimensional planar structure of graphene after N doping, albeit with more wrinkles at the edge of graphitic sheets. The EDX elemental mappings of carbon, oxygen, nitrogen in NG600 are shown in Fig. S1. The doped nitrogen is uniformly distributed over the graphene sheet of NG600.

The XRD patterns of GO, RGO600 and NGs are shown in Fig. 2(a). It was observed that the GO had a strong peak at  $2\theta = 11^\circ$ , corresponding to the (002) crystalline plane, indicating a well-ordered and layered structure. This is commensurate with a c-axis interlayer spacing of 0.8 nm. After reduction, RGO600 had a strong peak at  $2\theta = 26^\circ$ , corresponding to the interlayer spacing of 0.3 nm. The decrease in the interlayer spacing of RGO is attributed to the removal of oxygen-containing functional groups and restoration of graphene network during annealing. After N doping, the strong peak at  $2\theta = 11^\circ$  of GO disappeared in the XRD spectra of NGs and a new strong peak at around  $2\theta = 26^\circ$  emerged. It is worth noting that NG400 still had a small peak at  $2\theta = 11^\circ$ , which might be due to the formation of carbon nitride from urea during NG400 synthesis process [35] (corresponding to tri-s-triazine unit peak with relatively high intensity found in NG400 FTIR



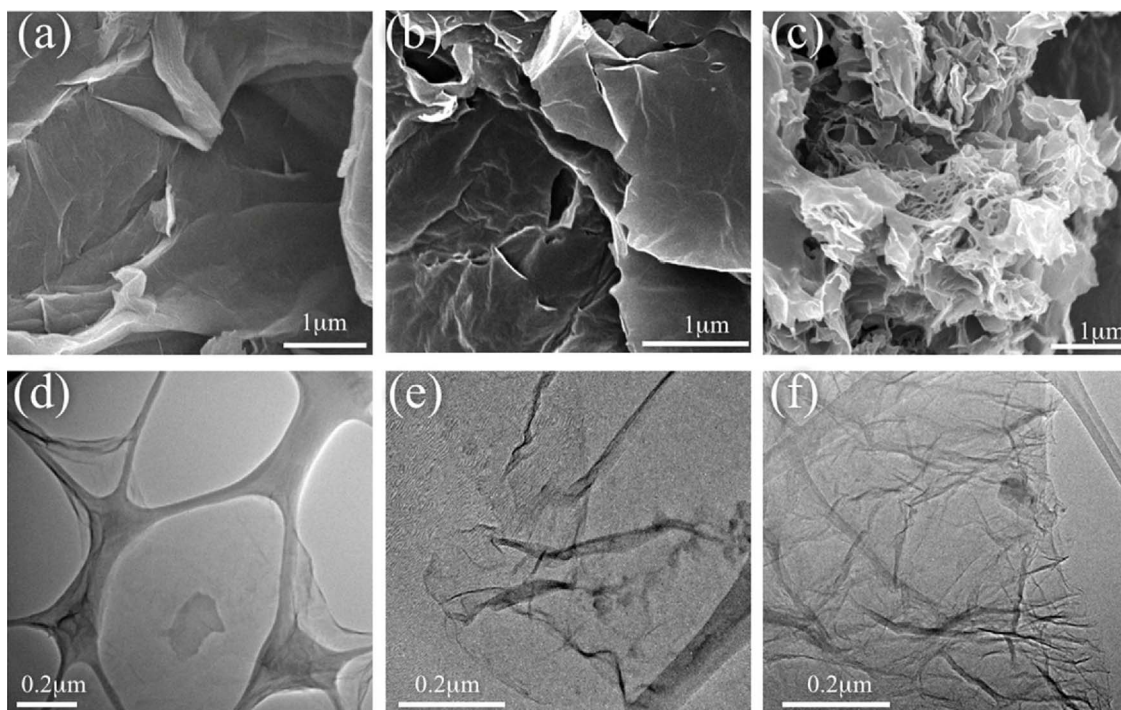


Fig. 1. FESEM images of GO (a), RGO600 (b) and NG600 (c). TEM images of GO (d), RGO600 (e) and NG600 (f).

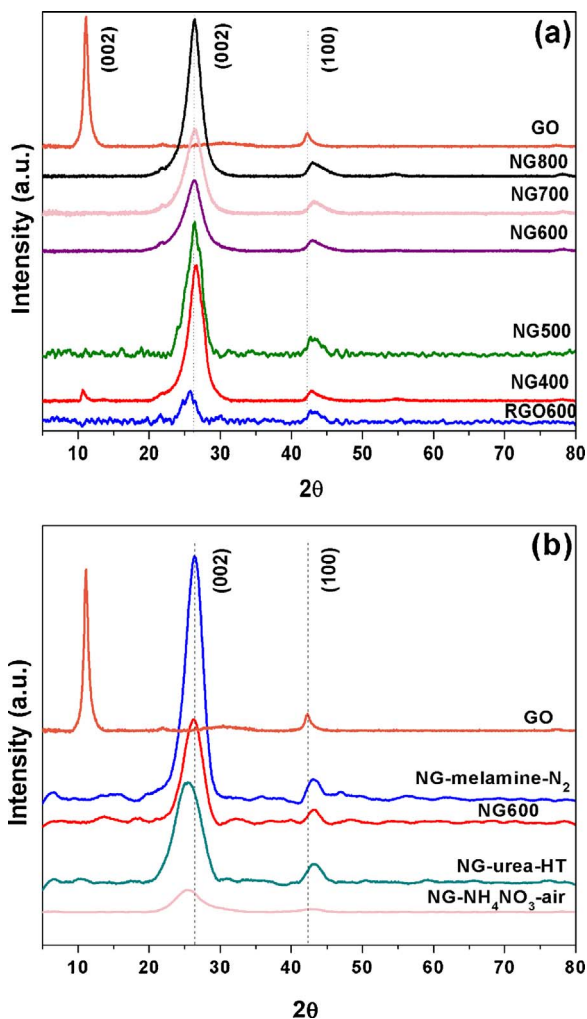


Fig. 2. XRD patterns of (a) GO, RGO600 and NG400–NG800, and (b) GO, NG600, NG-melamine- $N_2$ , NG-urea-HT and NG- $NH_4NO_3$ -air.

spectrum (Fig. 6(a)). Besides, compared with the peak of GO at  $2\theta = 42.3^\circ$ , which relates to (100) reflection, all the NGs had an up-shifted  $2\theta$  degrees ( $42.4^\circ$ – $43.2^\circ$ ), which indicates deoxygenation due to the elimination of oxygen-containing functional groups and successful N doping.

The chemical compositions of GO, RGO600 and NGs are shown in Table 1 and Fig. 3(a). From NG400 to NG800, the O/C atomic ratio decreased as the thermal annealing temperature increased, which suggests an enhancement of reduction level due to more oxygen-containing functional groups being eliminated at higher thermal annealing temperatures. Meanwhile, NG400 with the lowest thermal stability among all the NGs had the relatively high weight loss between 400 and 500°C due to the deoxygenation (Fig. S2(a)), further substantiating the relationship between thermal annealing temperature and the reducibility of NG. A decreasing trend of N/C atomic ratio was observed as the thermal annealing temperature increased from 400°C to 800°C, owing to the scission of C–N bond at the higher thermal annealing temperature or the desorption of amine and amide from NG [26].

The high-resolution N1s XPS spectra (in a narrow range of 394–407 eV) were obtained for all NGs (Fig. 4). The N signals can be deconvoluted into four types of N bonding configurations: pyridinic N (397.6 eV), pyrrolic N (399.2 eV), graphitic N (400.9 eV) and nitric oxide (N–O, 402.7 eV). As shown in Table 1 and Fig. 3(b), all four types of N bonding configurations were detected in the NGs prepared at  $T \geq 600^\circ\text{C}$ , while the NGs prepared at  $T \leq 500^\circ\text{C}$  possessed only three types of N bonding configurations (pyridinic N, pyrrolic N and graphitic N). More graphitic N was doped in the graphitic carbon network, increasing from 1.85 to 36.5%N ( $N_{\text{graphitic}}/N_{\text{total}}$  (%)), as the annealing temperature increased from 400 to 800°C. More nitric oxide (N–O) was also incorporated into the graphitic platelets, increasing from 3.94 to 9.60%N ( $N_{\text{nitricoxide}}/N_{\text{total}}$  (%)), as the annealing temperature increased from 600 to 800°C. These phenomena could be attributed to the higher thermal stability of graphitic N and nitric oxide than pyrrolic N. The increase in annealing temperature also resulted in the decrease of the O/C atomic ratio (Table 1) suggesting that simultaneous N doping and reduction occurred during the thermal annealing process. Meanwhile, the defective sites in the NG interlayer can be occupied by excess oxygen-containing functional groups via a stereo-hindrance effect [36]. Thus, a minor amount of oxygen-containing functional groups such as

**Table 1**  
Structure and chemical information of GO, RGO600 and NGs.

	N wt%	O/C at. %	N/C at. %	I <sub>D</sub> /I <sub>G</sub>	Pyridinic N N <sub>pyridinic</sub> /N <sub>total</sub> (%)	Pyrrolic N N <sub>pyrrolic</sub> /N <sub>total</sub> (%)	Graphitic N N <sub>graphitic</sub> /N <sub>total</sub> (%)	Nitric oxide N <sub>nitricoxide</sub> /N <sub>total</sub> (%)	C=O O <sub>C=O</sub> /O <sub>total</sub> (%)
GO	–	76.1	–	0.91	–	–	–	–	17.9
RGO600	–	11.1	–	0.94	–	–	–	–	23.0
NG400	30.2	12.5	44.6	1.10	54.5	43.6	1.85	–	44.9
NG500	24.2	9.80	31.7	1.11	49.2	42.6	8.27	–	44.9
NG600	16.0	8.00	18.3	1.12	38.4	31.8	25.9	3.94	43.7
NG700	13.7	7.20	15.0	1.09	33.6	21.2	37.5	7.71	43.6
NG800	11.6	6.60	12.4	1.10	32.8	21.1	36.5	9.60	41.8
NG-melamine-N <sub>2</sub>	19.3	8.80	23.1	1.04	52.8	34.5	12.8	–	38.4
NG-urea-HT	10.6	21.8	13.7	1.07	69.2	25.6	5.18	–	39.4
NG-NH <sub>4</sub> NO <sub>3</sub> -air	4.82	48.0	7.7	1.01	31.0	63.6	5.45	–	47.5

Weight percentages of carbon, nitrogen and oxygen were analyzed by CHNS/O analyzer. Atomic percentages of pyridinic N, pyrrolic N, graphitic N, nitric oxide and C=O were analyzed by XPS.

C=O group can also activate PMS. In this study, the content of C=O gradually decreased from 44.9 to 41.8% O (O<sub>C=O</sub>/O<sub>total</sub> (%)) with the increasing annealing temperature from 400 to 800 °C (Table 1 and Fig. S3(III)). Hence, the N doping level and reactive functional groups (e.g., pyridinic N, pyrrolic N, graphitic N and C=O) were successfully tailored by varying the thermal annealing temperature.

The degree of graphitization and doping status of graphene can be revealed by Raman spectra. The D band (~1350 cm<sup>-1</sup>) reflects the defective level of graphene platelets caused by zigzag/armchair edges,

vacancies, functional groups and heteroatom doping. Vacancies are easier to adsorb PMS than edging sites but have a lower electron-transfer capability from graphene to PMS for PMS activation. Zigzag/armchair edges can activate PMS to produce SO<sub>4</sub><sup>•-</sup> and HO<sup>•</sup> via peroxide O–O bond cleavage [36]. The G band (~1580 cm<sup>-1</sup>) is associated with E<sub>2g</sub> mode vibration of the intact honeycomb-like sp<sup>2</sup> hybridized carbon network [37]. The ratio of I<sub>D</sub>/I<sub>G</sub> reveals the defective degree of carbon materials. As shown in Table 1 and Fig. 5(a), all the NGs had higher ratios of I<sub>D</sub>/I<sub>G</sub> (1.09–1.12) than those of GO (0.91) and RGO600 (0.94), indicating more defective sites and sp<sup>3</sup> C atoms generated, which might be ascribed to the introduction of N dopant, the loss of C atoms owing to the elimination of oxygen-containing functional groups, and the creation of smaller-sized nanocrystalline graphitic domains [38]. The discrepancy in the position of G band has been reported. Lin et al. [39] reported a downshift of G peak after N doping. Pyridinic N and pyrrolic N, which introduce p-type doping, lead to an upshift of G peak. In contrast, graphitic N, which introduces n-type doping, downshifts the G peak. Li et al. [40] proposed an upshift of G peak after N doping. In this study, an upshift of G peak after N doping was observed. And this upshift at the low thermal annealing temperature can be mainly ascribed to the higher N content in NG, while the constricted C–C bond and increased bond vibration frequency due to the introduced defects can account for the upshift of G peak at the higher thermal annealing temperature [41].

The functional groups of GO, RGO600 and NGs were analyzed by FTIR. As displayed in Fig. 6(a), GO showed characteristic peaks at 1740 cm<sup>-1</sup> (C=O (COOH) stretching vibration), 1620 cm<sup>-1</sup> (C=C), 1403 cm<sup>-1</sup> (tertiary alcoholic C–OH bending), 1223 cm<sup>-1</sup> (C–O (epoxy)), 1091 cm<sup>-1</sup> (C–O (alkoxy) stretching vibration) and a broad peak at 3413 cm<sup>-1</sup> (the vibration of O–H or water molecules). After N doping, the dramatic reduction in the intensities of C=O and C–O groups indicates the intensive deoxygenation due to the removal of surface oxygen-containing functional groups, which is consistent with the O/C atomic ratio analysis and substantiated by the reduction in the thickness of NG (Fig. S4). The broad peak at 3413 cm<sup>-1</sup> disappeared, suggesting an increment in hydrophobicity of NG. The C=C bond of NG shifted to a lower wavenumber (1553 cm<sup>-1</sup>). A new peak at 1175 cm<sup>-1</sup> emerged due to the formation of C–N bond and the residual C–O bond [39]. It is worth noting that a small peak at 785 cm<sup>-1</sup> appeared at the FTIR spectra of NG400 and NG500 (NG500 had a lower peak intensity than NG400) which might be ascribed to the formation of tri-s-triazine (a type of nitrogen-containing heterocycle that is not conducive to PMS activation) [42].

The SSA, pore volume and pore size distribution of GO, RGO600 and NGs are shown in Table 2 and Fig. S5(a) and (b). GO possessed a low SSA (26 m<sup>2</sup> g<sup>-1</sup>) and pore volume (0.017 cm<sup>3</sup> g<sup>-1</sup>) probably due to the severe stacking effect resulted from the strong hydrogen bonding formed between oxygen-containing functional groups on the GO layers. Thermal annealing can not only reduce the oxygen-containing

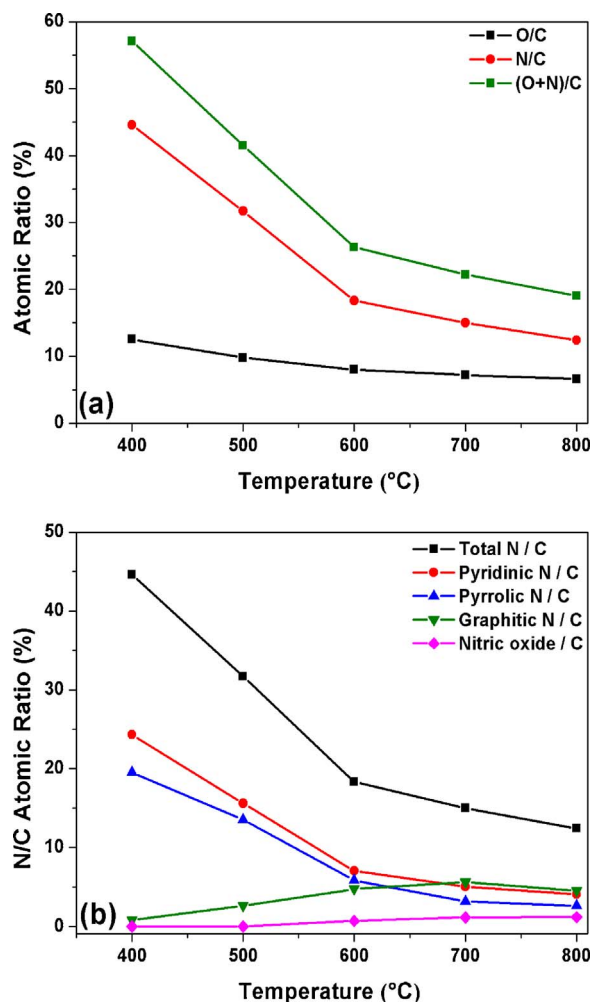


**Fig. 3.** Variation of nitrogen and oxygen contents (a) and variation of total N, pyridinic N, pyrrolic N, graphitic N and nitric oxide contents (b) of NG400-NG800 with thermal annealing temperature.

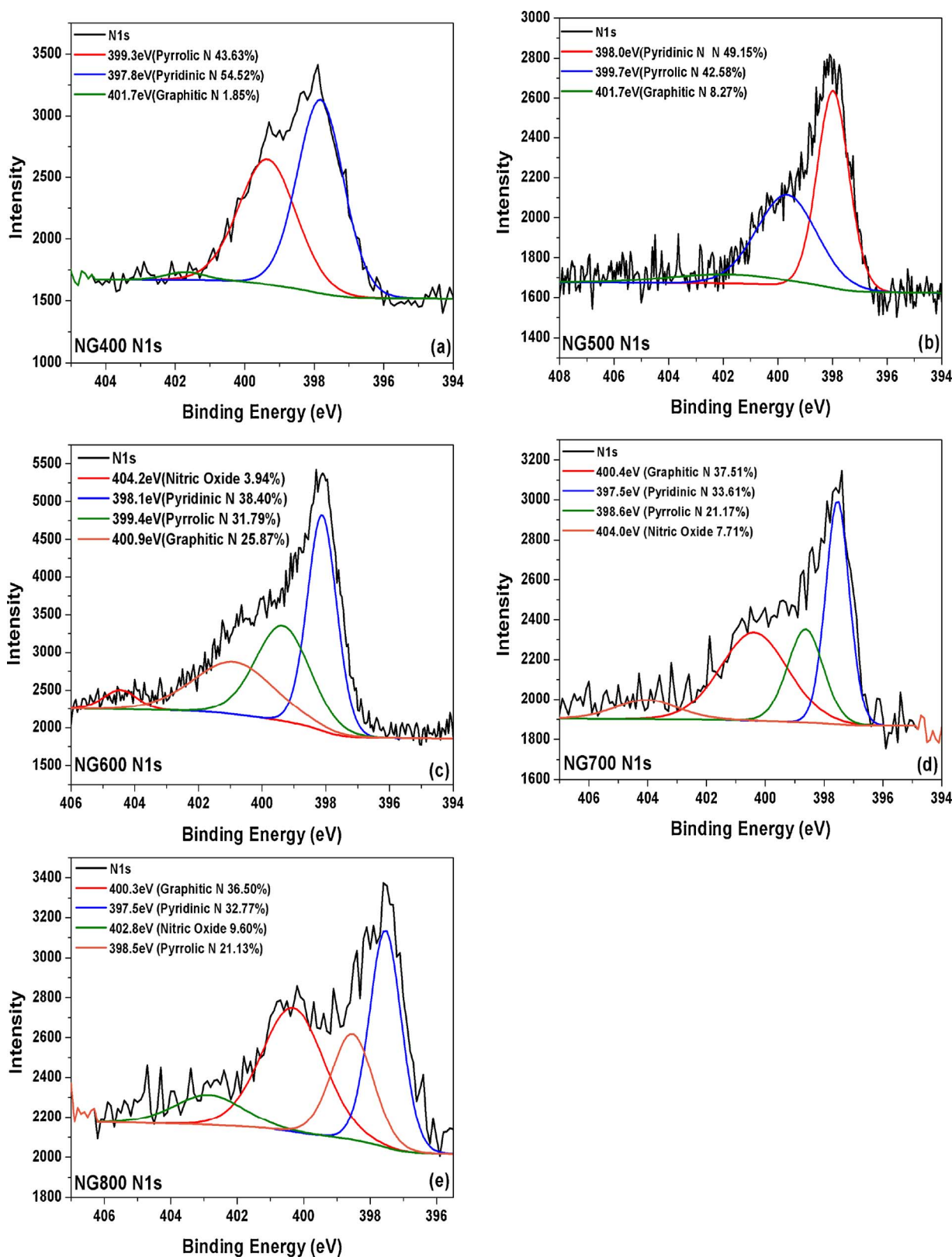


Fig. 4. N1s scans of NG400 (a), NG500 (b), NG600 (c), NG700 (d) and NG800 (e).

functional groups, but also result in thermal expansion. Thus, RGO600 had the highest SSA ( $452 \text{ m}^2 \text{ g}^{-1}$ ) and pore volume ( $0.441 \text{ cm}^3 \text{ g}^{-1}$ ). The SSA and pore volume of NG400-NG800 increased with the increasing thermal annealing temperature.

### 3.1.2. NGs prepared with different synthesis methods

For comparison, other NGs were also prepared using various synthesis methods found in the literature, namely NG-melamine- $\text{N}_2$ , NG-urea-HT and NG- $\text{NH}_4\text{NO}_3$ -air. The morphologies of NGs were analyzed by FESEM (Fig. S6). More exfoliation of NGs was formed after N doping for all the



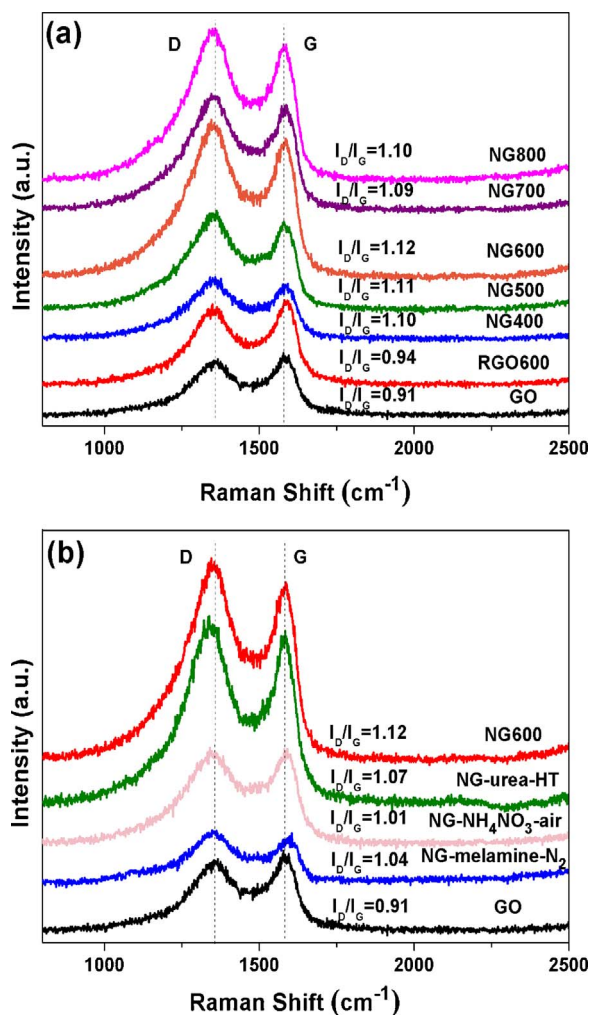


Fig. 5. Raman spectra of (a) GO, RGO600 and NG400-NG800, and (b) GO, NG600, NG-melamine-N<sub>2</sub>, NG-urea-HT and NG-NH<sub>4</sub>NO<sub>3</sub>-air.

NGs. As shown in Table 1, the O/C atomic ratios followed the order of NG600 < NG-melamine-N<sub>2</sub> < NG-urea-HT < NG-NH<sub>4</sub>NO<sub>3</sub>-air, indicating a higher reducibility caused by thermal annealing at a higher temperature under an inert condition with urea as a nitrogen source than hydrothermal and low temperature combustion methods (with mild synthesis condition) or thermal annealing with melamine as a nitrogen source. NG600 had the highest content of graphitic N ( $N_{\text{graphiticN}}/N_{\text{total}}$  (%)) with the higher thermal stability in the carbon network (25.9%N of NG600 and 12.8%N of NG-melamine-N<sub>2</sub>, respectively) than that of NG-urea-HT and NG-NH<sub>4</sub>NO<sub>3</sub>-air (5.18 and 5.45%N, respectively) (Fig. S3(II)). Milder synthesis methods or adoption of melamine as a nitrogen source are inefficacious to produce desirable N bonding configurations.

The XRD spectra are shown in Fig. 2(b). The higher intensity of the characteristic GO peak at  $2\theta = 42^\circ$  reflects the restoration of a well-ordered sp<sup>2</sup> hybridized carbon network, which can be interrupted by the formation of sp<sup>3</sup> hybridized C such as C–O bond [43]. The NG-NH<sub>4</sub>NO<sub>3</sub>-air having the lowest reducibility (the highest O/C atomic ratio) among NGs might account for its lowest peak intensity at  $2\theta = 42^\circ$ . The FTIR spectra are shown in Fig. 6(b). It is worth noting that NG-NH<sub>4</sub>NO<sub>3</sub>-air still had a weak peak at 1740 cm<sup>-1</sup> attributable to C=O, which is commensurate with NG-NH<sub>4</sub>NO<sub>3</sub>-air having the lowest reducibility among NGs. A small peak at 785 cm<sup>-1</sup> appeared at the FTIR spectrum of NG-melamine-N<sub>2</sub> which might be ascribed to the formation of tri-s-triazine. As shown in Table 2 and Fig. S5(c) and (d), hydrothermal method can increase the SSA dramatically, resulting in

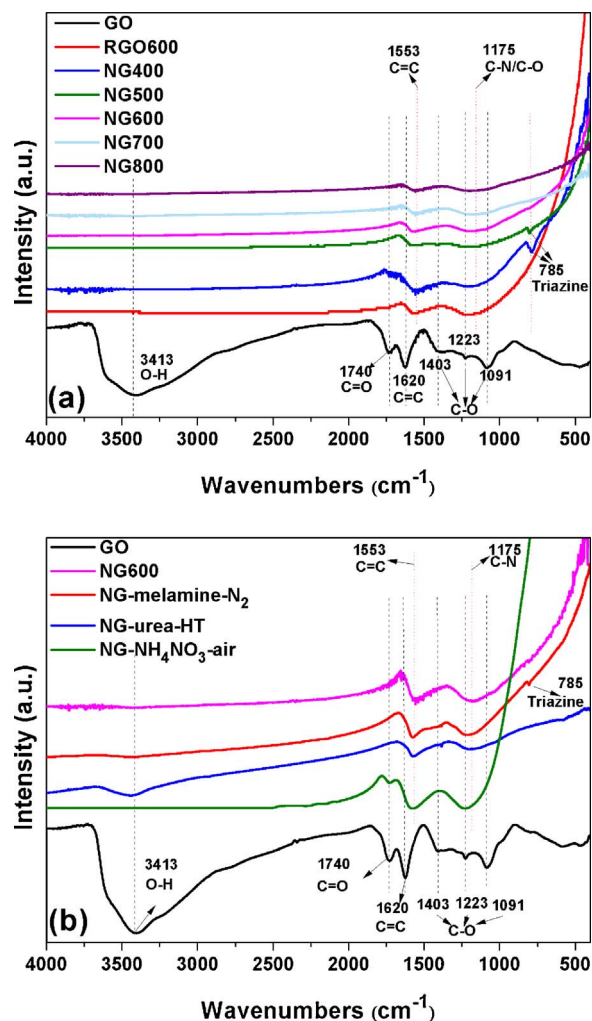


Fig. 6. FTIR transmittance spectra of (a) GO, RGO600 and NG400-NG800, and (b) GO, NG600, NG-melamine-N<sub>2</sub>, NG-urea-HT and NG-NH<sub>4</sub>NO<sub>3</sub>-air.

Table 2  
SSA, pore volume and pore size information of GO, RGO600 and NGs.

Catalyst	BET SSA (m <sup>2</sup> g <sup>-1</sup> )	Average pore volume <sup>a</sup> (cm <sup>3</sup> g <sup>-1</sup> )	Average pore size <sup>b</sup> (nm)
GO	26	0.017	2.03
RGO600	452	0.441	2.02
NG400	25	0.060	2.03
NG500	24	0.056	2.03
NG600	74	0.164	2.02
NG700	131	0.238	2.01
NG800	140	0.243	2.03
NG-melamine-N <sub>2</sub>	8	0.0168	2.03
NG-urea-HT	515	0.385	2.02
NG-NH <sub>4</sub> NO <sub>3</sub> -air	93	0.191	2.03

<sup>a</sup> BJH method cumulative desorption pore volume.

<sup>b</sup> BJH method desorption pore radius (Mode D<sub>v</sub>(r)).

NG-urea-HT with a higher SSA and pore volume than thermal annealing and low temperature combustion methods.

### 3.2. Catalytic performance of NGs

The performance of NG as a PMS activator for SAM degradation was evaluated in the aqueous solution at pH 7 (close to the pH value of real water matrix). In general, for GO and NGs, about 20% of SAM removal was due to the adsorption process (Figs. 7 (a) and 8 (a)). The RGO600

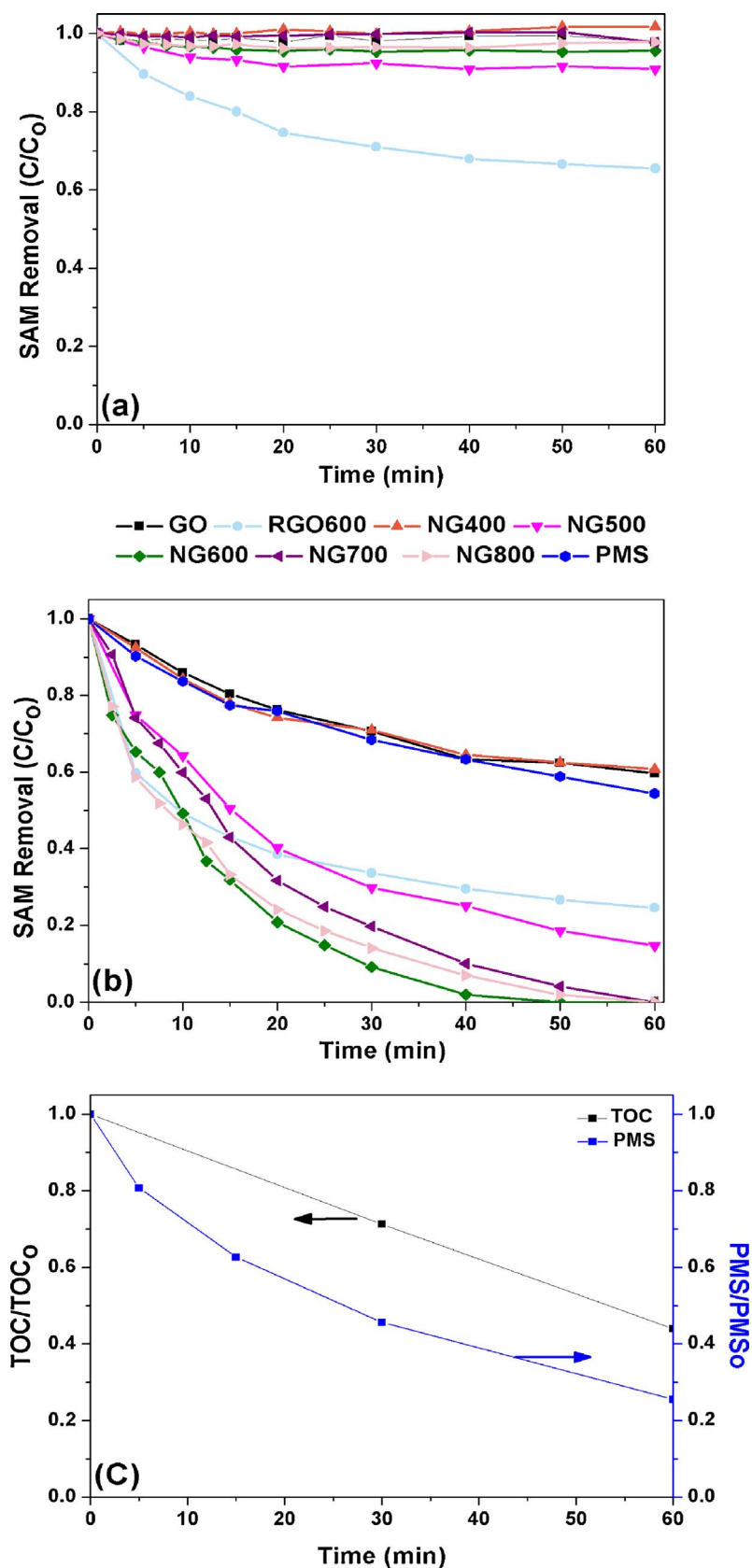


Fig. 7. Adsorption performances (a) and catalytic performances (b) of catalysts prepared at different thermal annealing temperatures. TOC removal and PMS consumption in the NG600/PMS system (c) (Condition: [PMS] = 0.5 mM, [SAM] = 10 mg L<sup>-1</sup>, [catalyst] = 0.2 g L<sup>-1</sup>, pH = 7).

exhibited the highest adsorption ability with 34% SAM removal efficiency, probably due to its relatively higher SSA (452 m<sup>2</sup> g<sup>-1</sup>) and favorable surface functional groups for adsorption process. Compared to the RGO600 (without N surface functionalization), the N doping

process in the NG can induce reduction as well as the incorporation of N atoms which reduces the  $\pi$ - $\pi$  stacking interaction between NG and SAM, leading to the poor adsorption performance of NG-urea-HT, albeit with a comparable high SSA (515 m<sup>2</sup> g<sup>-1</sup>).



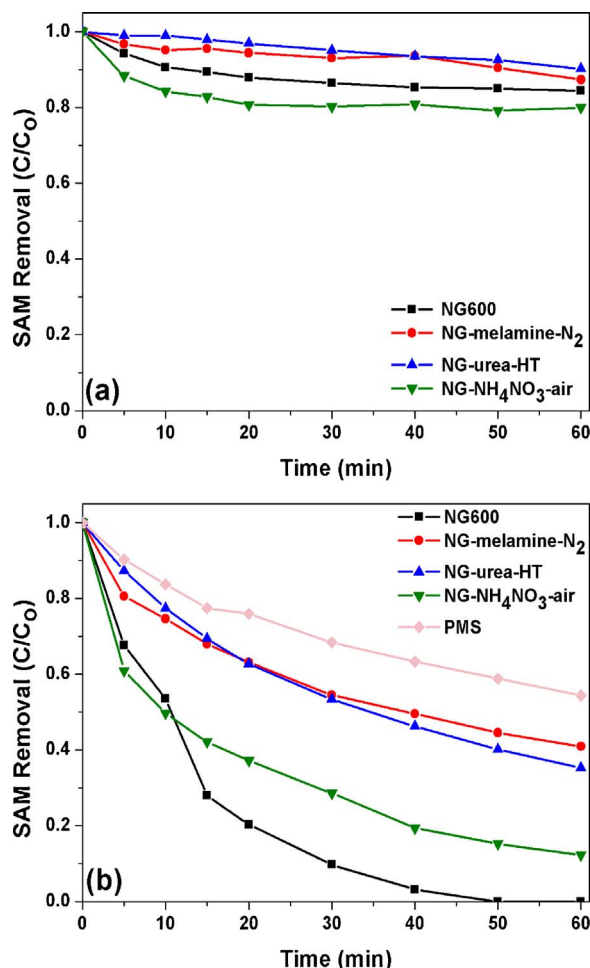


Fig. 8. Adsorption performances (a) and catalytic performances (b) of catalysts prepared via different synthesis methods (Condition: [PMS] = 0.5 mM, [SAM] = 10 mg L<sup>-1</sup>, [catalyst] = 0.2 g L<sup>-1</sup>, pH = 7).

### 3.2.1. Catalytic performance of NGs prepared with different temperatures

Fig. 7(b) shows the catalytic activity of NGs fabricated with different synthesis temperatures. Direct PMS oxidation contributed to ~40% SAM removal efficiency within 60 min. The apparent first order reaction rate constant ( $k_{app}$ ) of SAM degradation via PMS activation by GO, RGO600 and NGs was estimated using the pseudo first-order kinetics as shown below:

$$\ln\left(\frac{C}{C_0}\right) = -k_{app}t \quad (1)$$

where  $C_0$  is the initial SAM concentration and  $C$  is the SAM concentration at time  $t$ .

The SAM degradation rate by direct PMS oxidation (0.0095 min<sup>-1</sup>), GO/PMS (0.0086 min<sup>-1</sup>) and NG400/PMS (0.0081 min<sup>-1</sup>) were comparable indicating that GO and NG400 can hardly activate PMS for SAM degradation. Meanwhile, RGO600 (0.019 min<sup>-1</sup>) exhibited 75% removal efficiency within 60 min, mainly due to its relatively higher adsorption efficiency. On the other hand, NG500, NG600, NG700 and NG800 exhibited catalytic activities for PMS activation. The performance of NGs prepared at different temperatures was in the following order: NG400 < NG500 < NG700 < NG800 < NG600. The poorer performance of NG400 (no significant catalytic activity) and NG500 (with 85% removal efficiency within 60 min) to activate PMS might be ascribed to: (1) the formation of tri-s-triazine (a type of nitrogen-containing heterocycle that is not conducive to PMS activation, which can be verified by the experiment for the comparison between g-C<sub>3</sub>N<sub>4</sub> (Text S1) and NG600 in activating PMS for SAM degradation, as shown in Fig.

S7) (2) the relatively lower amount of graphitic N, and (3) the relatively small SSA (25 and 24 m<sup>2</sup> g<sup>-1</sup> for NG400 and NG500, respectively). The NG600 exhibited the highest catalytic activity with 100% SAM removal efficiency, 58% TOC removal, and 74% PMS consumption within 60 min (Fig. 7(c)). The SAM degradation by NG600/PMS is 5 and 10 times faster than that of RGO/PMS and GO/PMS, respectively, indicating the catalytic activity of NG could be attributed to the N functional groups developed during N doping process. During NG synthesis, amino groups in the urea reacted with oxygen-containing functionalities on the GO surface (e.g., -OH and C=O). N atom was incorporated into the edges of carbon lattice to form pyridinic N and pyrrolic N first. As the thermal annealing temperature increased, pyridinic N and pyrrolic N could be transformed into graphitic N [44]. Meanwhile, NH<sub>3</sub> and CO<sub>2</sub> would be released from the decomposition of urea to produce porous structure as well as N-doping. Urea was reported to yield low carbon nitride during pyrolysis [45] and a slow ramping rate (5 °C min<sup>-1</sup>) adopted in this study suppressed the formation of carbon nitride at thermal annealing temperature of ≥ 600 °C [46]. Meanwhile, the N doping level and reactive functional groups to activate PMS can be tailored by changing the thermal annealing temperature. Therefore, NG600 possesses a higher N doping level (16.0 wt%) and an optimal amount of pyridinic N (38.4%N), pyrrolic N (31.8%N), graphitic N (25.9%N) and C=O groups (43.7%O) (Table 1), inducing SAM degradation via the best combination of radical and non-radical pathways. These factors contribute to the outstanding catalytic performance of NG600/PMS. The degradation of other antibiotics, namely SNM, SMX, and STZ in the NG600/PMS system were also investigated (Fig. S8). The NG600/PMS system can remove these pollutants (> 95% removal efficiency) within 60 min, indicating that the NG600 is a promising carbocatalyst for sulfonamide antibiotics removal.

### 3.2.2. Catalytic performance of NGs prepared with different synthesis methods

Fig. 8(b) compares the catalytic activities of NGs fabricated by different synthesis methods. The performance of the NGs (SAM removal efficiency,  $k_{app}$ ) was in the order of NG600 (100%, 0.090 min<sup>-1</sup>) > NG-NH<sub>4</sub>NO<sub>3</sub>-air (88%, 0.032 min<sup>-1</sup>) > NG-urea-HT (65%, 0.017 min<sup>-1</sup>) > NG-melamine-N<sub>2</sub> (59%, 0.014 min<sup>-1</sup>). Thermal annealing temperature of > 600 °C is required for the decomposition of carbon nitride formed during NG-melamine-N<sub>2</sub> synthesis process, and the following incorporation of N atom into the graphitic sheets by the interaction between the formed N species during carbon nitride decomposition and active sites on GO [47]. Thus, the thermal annealing temperature of 600 °C adopted in the present study is not high enough to decompose carbon nitride. Besides, the SSA of NG-melamine-N<sub>2</sub> (8 m<sup>2</sup> g<sup>-1</sup>) (Table 2 and Fig. S5(c)) is too small to provide necessary active sites for PMS activation. These two factors may mainly account for the poorest PMS activation performance of NG-melamine-N<sub>2</sub> for SAM degradation even with the highest N doping level (19.3 wt%) (Table 1), which can be substantiated by the tri-s-triazine peak detected in the FTIR spectra (Fig. 6(b)).

The NG-NH<sub>4</sub>NO<sub>3</sub>-air with the lowest N doping level of 4.82 wt.% exhibited superior catalytic performance, i.e., ~2 times better than that of NG-melamine-N<sub>2</sub> or NG-urea-HT. The decomposition of NH<sub>4</sub>NO<sub>3</sub> during synthesis released NH<sub>3</sub> which acts as a doping agent together with other gases like N<sub>2</sub> or N<sub>2</sub>O, resulting in the NG with a porous structure and a large SSA (93 m<sup>2</sup> g<sup>-1</sup>) (Table 2 and Fig. S5(c)). As shown in Table 1, NG-NH<sub>4</sub>NO<sub>3</sub>-air possessed higher densities of pyrrolic N and pyridinic N than that of graphitic N. It was reported that the abundant free-flowing  $\pi$ -electrons from sp<sup>2</sup> graphitic plane can be activated through conjugating with the lone-pair electrons of N dopants to induce PMS activation and production of free radicals, and N functionalities at the edge (rather than graphitic N) improved the catalytic ability via PMS activation [21].

The best SAM degradation performance of NG600 among the NGs might be due to reasons: (1) NG600 had a higher N doping level and an

optimal amount of reactive functional groups (pyridinic N, pyrrolic N, graphitic N and C=O group) effective for both radical and non-radical pathway (Table 1); (2) NG600 had the highest  $I_D/I_G$  value (1.12) and relatively lower O/C atomic ratio (8.00%) (Table 1 and Fig. 5(b)), indicating more defective sites have been created for PMS activation due to N doping and removal of oxygen-containing functional groups; (3) NG600 had a relative high SSA ( $74 \text{ m}^2 \text{ g}^{-1}$ ) (Table 2 and Fig. S5(c)) to provide a higher density of active sites for PMS activation. However, the SSA contributes less significantly than N doping to the degradation performance. The highest SSA of NG-urea-HT ( $515 \text{ m}^2 \text{ g}^{-1}$ ) (Table 2 and Fig. S5(c)) does not endow it with the best catalytic performance for SAM degradation via PMS activation. Therefore, the NG600 synthesis method adopted in this research makes an improvement in controlling N bonding configurations and is superior in producing a good PMS activator over other optimized methods found in the literature.

### 3.3. Effects of PMS dosage, catalyst loading and common matrix species

Since NG600 showed the best catalytic performance to activate PMS for SAM degradation, NG600 was selected for further kinetics study. To investigate the effect of PMS dosage on the catalytic performance of NG via PMS activation, 0.2, 0.5 and 0.9 mM PMS dosages were used and the corresponding molar ratios of PMS: SAM were 3.5:1, 10:1 and 20:1, respectively. Fig. 9(a) shows that the SAM degradation rate of NG600 increases linearly from  $k_{app} = 0.020$  to  $0.19 \text{ min}^{-1}$  with the increasing PMS dosage from 0.20 to 0.90 mM. The better catalytic performance at the higher PMS dosage can be attributed to increased interaction between PMS and catalysts, which is conducive to SAM degradation via both radical generation and non-radical pathways.

Fig. 9(b) reveals that the catalytic activity of NG600 increases linearly from  $0.015$  to  $0.020 \text{ min}^{-1}$  with the increasing catalyst loading from  $0.1$  to  $0.3 \text{ g L}^{-1}$ . A higher catalyst loading can provide more active sites for PMS activation, thus elevating the SAM degradation rate. The slopes of the linear plot in insets of Fig. 9(a) and (b) demonstrate that an increase in the catalyst loading improves SAM degradation 4 times more than an increase in the PMS dosage. Given it is easier to recover and recycle NG than PMS, it is operationally more economical to improve the SAM degradation by increasing catalyst loading than PMS dosage in the NG/PMS system.

Fig. 9(c) presents the effects of several common matrix species, namely  $\text{Cl}^-$ ,  $\text{NO}_3^-$  and humic acid, on SAM degradation. The concentrations of the common matrix species were selected based on the real secondary wastewater effluent [48]. While  $\text{NO}_3^-$  exhibited an insignificant effect on SAM degradation in the NG600/PMS system,  $\text{Cl}^-$  and humic acid affected the SAM degradation a little bit more negatively, leading to 17%, 28% decreases in the  $k_{app}$  values, respectively. The  $\text{Cl}^-$  is a relatively strong  $\text{SO}_4^{\cdot-}$  scavenger with pseudo-second order rate constant of  $k_{\text{SO}_4^{\cdot-}+\text{Cl}^-} = 3.0 \times 10^8 \text{ M}^{-1} \text{ s}^{-1}$  [49,50]. Similarly, humic acid consists of organic matters with carbon and oxygen-based moieties which can react with the generated reactive oxygen species (ROS), thus inhibiting the SAM degradation.

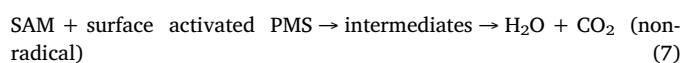
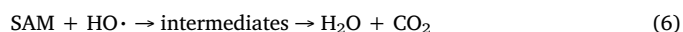
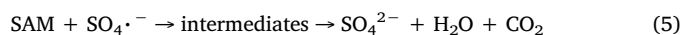
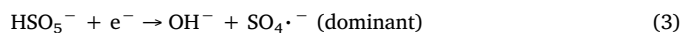
### 3.4. Mechanism of PMS activation by NG/PMS system

Radical pathway can be triggered by several aspects as follows: (1) the active sites on the NG (e.g., vacancies, zigzag/armchair edges) with delocalized  $\pi$  electrons [11,36]; (2) Lewis basic sites with lone-pair electrons such as pyridinic N, pyrrolic N and ketonic groups [51]; (3) the abundant free-flowing  $\pi$ -electrons from  $\text{sp}^2$  carbons of graphene which can be activated through conjugating with the lone-pair electrons of N dopants [21]. These sites can function as electron donors, which transfer electrons to activate PMS by O–O bond cleavage and thereby produce  $\text{SO}_4^{\cdot-}$  and  $\text{HO}^{\cdot}$ . Then pollutants (electron donor) can be oxidized into  $\text{CO}_2$  and  $\text{H}_2\text{O}$  by  $\text{SO}_4^{\cdot-}$  and  $\text{HO}^{\cdot}$  (electron acceptor). Non-radical pathway refers to organic pollutants degradation via the direct electron transfer without production of radicals. PMS is adsorbed

on electron-rich  $\text{sp}^2$  sites of graphitic domain (especially graphitic N) first due to outer-sphere interaction (electrostatic bonding). PMS can be activated by the  $\text{sp}^2$  carbon network to form surfaced activated PMS with a slight rearrangement of PMS electrons (without PMS dissociation into radicals). Then the surface activated PMS (electron acceptor) can readily react with the adsorbed organic pollutant (electron donor) resulting in PMS consumption. Thus, for the NG/PMS system, non-radical pathway works through forming outer-sphere complexes between NG and PMS to facilitate pollutant degradation, which can be significantly hampered by the increase in the ionic strength of the reaction system [28].

To investigate the possible PMS activation mechanism in the NG/PMS system, chemical scavenger (with phenol,  $\text{NaClO}_4$  and nitrobenzene (NB) as ROS scavengers) and EPR were employed to determine the dominant pathway contributing to SAM degradation. In the radical scavenger method, phenol was used to scavenge both  $\text{SO}_4^{\cdot-}$  and  $\text{HO}^{\cdot}$  ( $k_{\text{SO}_4^{\cdot-}+\text{phenol}} = 8.8 \times 10^9 \text{ M}^{-1} \text{ s}^{-1}$ ,  $k_{\text{HO}^{\cdot}+\text{phenol}} = 6.6 \times 10^9 \text{ M}^{-1} \text{ s}^{-1}$ ) [52,53]. Besides, phenol is more hydrophobic than ethanol or methanol to approach the NG catalyst surface to trap  $\text{SO}_4^{\cdot-}$  and  $\text{HO}^{\cdot}$ . The NB acts as a  $\text{HO}^{\cdot}$  scavenger ( $k_{\text{HO}^{\cdot}+\text{NB}} (3.9 \times 10^9 \text{ M}^{-1} \text{ s}^{-1}) > k_{\text{SO}_4^{\cdot-}+\text{NB}} (< 10^6 \text{ M}^{-1} \text{ s}^{-1})$ ) [54,55]. Meanwhile,  $\text{NaClO}_4$  can contribute to the ionic strength of the NG/PMS system without inducing PMS activation and thus can act as an inhibitor for non-radical pathway.

As shown in Fig. 10 and Table S2, in the NG600/PMS system, only 18% SAM removal was achieved at a phenol/SAM molar ratio of 1000:1 within 60 min. However, 75% SAM removal can be achieved at a  $\text{NaClO}_4$ /SAM molar ratio of 17000:1 within 60 min. Meanwhile, there was still a high SAM removal efficiency (87%) within 60 min when adding NB to suppress  $\text{HO}^{\cdot}$ . The addition of phenol hampered the SAM degradation ( $0.003 \text{ min}^{-1}$ ) much more significantly than that of NB ( $0.033 \text{ min}^{-1}$ ) or  $\text{NaClO}_4$  ( $0.023 \text{ min}^{-1}$ ). Furthermore, the results of the EPR study are presented in Fig. S9. As shown in Fig. S9(a), there were no obvious characteristic signals present in the EPR spectra of experiments conducted with (i) DMPO and (ii) PMS + SAM + DMPO systems, respectively. However, in the NG600/PMS system, the characteristic signals of 5,5-dimethyl-2-pyrrolidone-N-oxyl (DMPOX) with heptet were detected, which were formed by the oxidation of DMPO, indirectly indicating that some strong ROS (e.g.  $\text{SO}_4^{\cdot-}$ ,  $\text{HO}^{\cdot}$ , etc.) were produced in the NG600/PMS system. The transformation of DMPO to DMPOX and the indirect indication of the existence of  $\text{SO}_4^{\cdot-}$  and  $\text{HO}^{\cdot}$  might be depicted by Fig. S9(b) [56,57].  $\text{DMPO} \cdot \text{SO}_4^{\cdot-}$  might react undesirably with  $\text{H}_2\text{O}$  via nucleophilic substitution reaction to yield  $\text{DMPO} \cdot \text{HO}^{\cdot}$  at a considerably fast reaction rate (e.g.  $t_{1/2}$  of  $\text{DMPO} \cdot \text{SO}_4^{\cdot-} = 95 \text{ s}$  in water) [58]. Besides,  $\text{SO}_4^{\cdot-}$  might work through electron extraction to facilitate the oxidation of  $\text{DMPO} \cdot \text{HO}^{\cdot}$  to form DMPOX. Based on the results of the chemical scavengers and EPR studies, it can be construed that (1) radical pathway contributed at least 3 times more to SAM degradation (based on the  $k_{app}$  values) in the NG600/PMS system than non-radical pathway, and (2) between  $\text{SO}_4^{\cdot-}$  and  $\text{HO}^{\cdot}$ , the former is the key contributor to SAM degradation. The proposed mechanism of PMS activation and SAM degradation on the NG is shown in Fig. 11 and Eqs. (2)–(7) as follows:



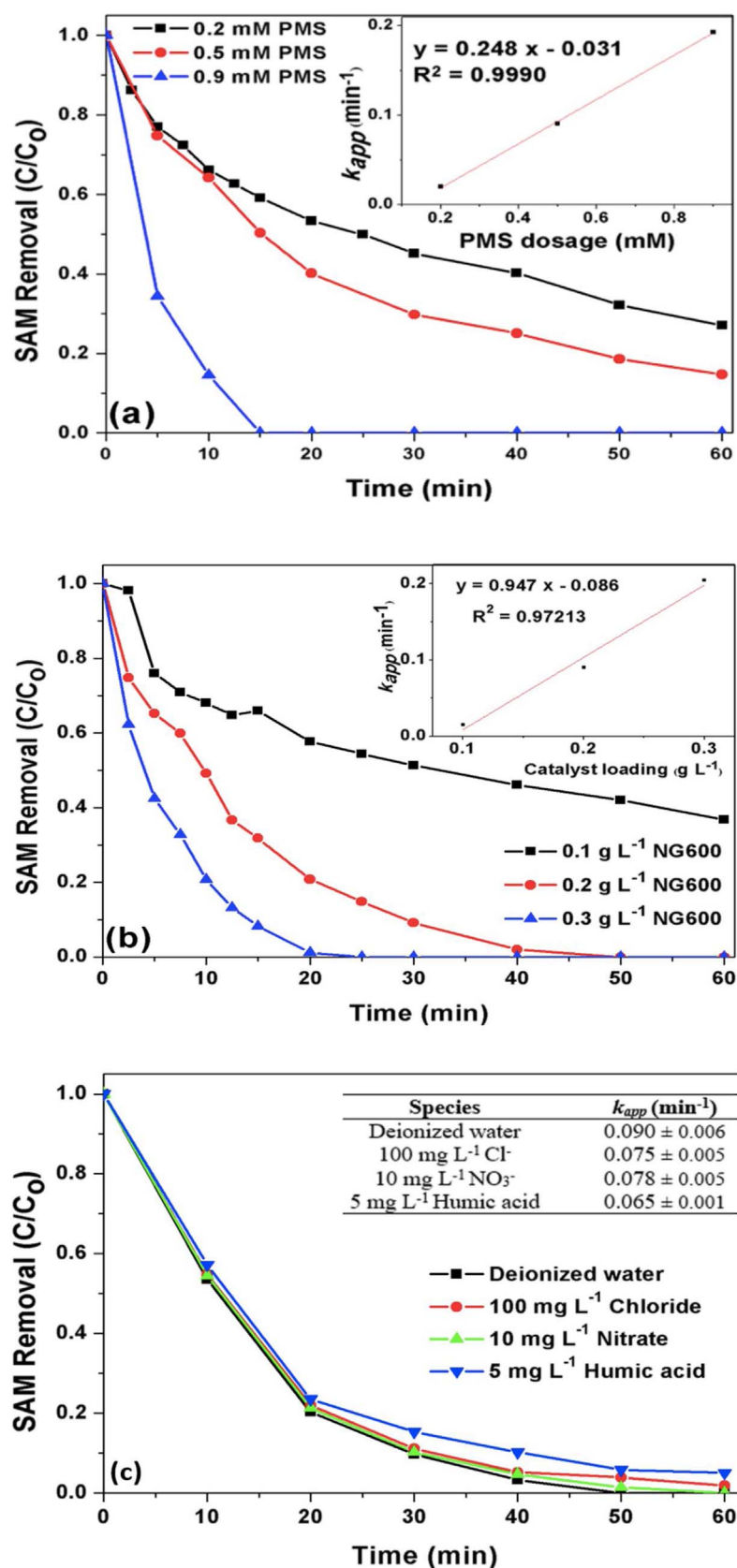


Fig. 9. The effect of (a) PMS dosage, (b) catalyst loading and (c) common matrix species on the SAM degradation by NG600 via PMS activation (Condition: [PMS] = 0.2, 0.5, 0.9 mM, [SAM] = 10 mg L<sup>-1</sup>, [catalyst] = 0.1, 0.2, 0.3 g L<sup>-1</sup>, [Cl<sup>-</sup>] = 100 mg L<sup>-1</sup>, [NO<sub>3</sub><sup>-</sup>] = 10 mg L<sup>-1</sup>, [humic acid] = 5 mg L<sup>-1</sup>, pH = 7). Inset of (a) and (b): the relationship between SAM degradation rate and PMS dosage (a) and catalyst loading (b).

### 3.5. Computational calculations

Density functional theory (DFT) calculations were adopted to give further insights into the PMS activation process on NG. Fig. 12 presents

structural information of adsorbed and free PMS based on DFT calculation. As shown in Fig. 12, after PMS being adsorbed on the graphitic N area of NG, the position of the peroxide O–O bond changed slightly, much closer to the graphitic sheet of NG. The binding energy ( $E_b$ )

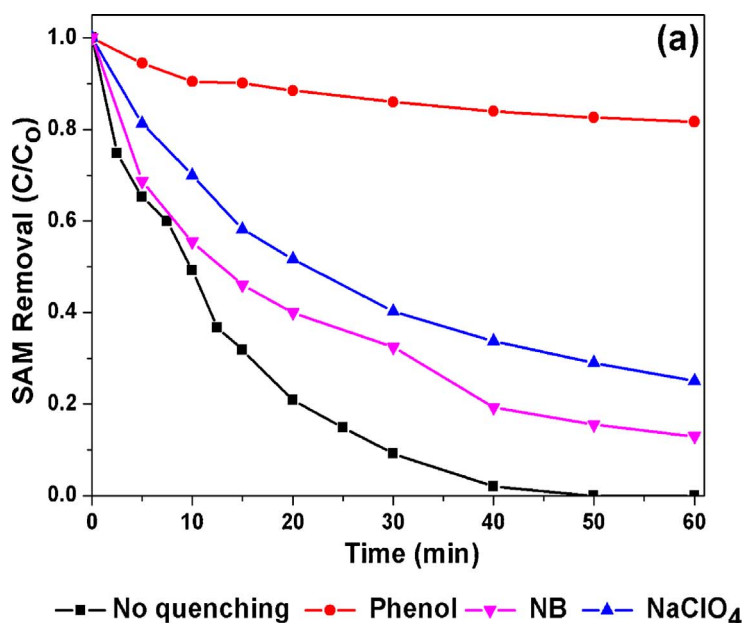
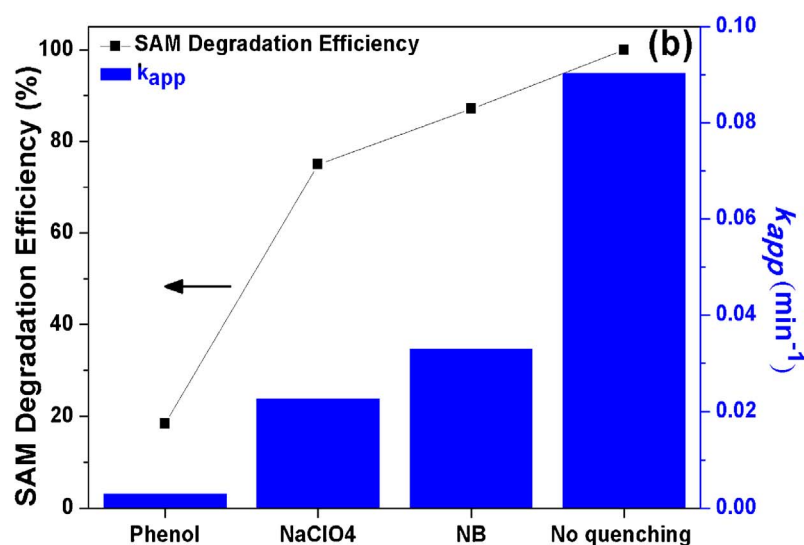


Fig. 10. The effect of phenol, NaClO<sub>4</sub> and NB as quenching agents on the SAM removal (a) and the SAM degradation rate and degradation efficiency (b) by NG600/PMS (Condition: [PMS] = 0.5 mM, [SAM] = 10 mg L<sup>-1</sup>, [catalyst] = 0.2 g L<sup>-1</sup>, pH = 7, the molar ratio of phenol: SAM = 1000:1, [NB] = 25 mg L<sup>-1</sup>, [NaClO<sub>4</sub>] = 0.8 M).



between PMS and NG was calculated by  $E_b = E_{\text{graphene} + \text{PMS}} - E_{\text{graphene}} - E_{\text{PMS}}$ , where  $E_{\text{graphene} + \text{PMS}}$ ,  $E_{\text{graphene}}$ ,  $E_{\text{PMS}}$  are total energies of graphene with PMS adsorption, graphene alone, and free PMS molecule, respectively. DFT calculation results for PMS activation on graphitic N are  $E_b = -2.78$  eV and  $Q = -0.908$  e (where  $Q$  is the number of electrons transferred between PMS and NG), which indicates the graphitic N can activate PMS through enhancing adsorption of PMS on NG and then form surface activated PMS with a slight rearrangement of electron structure of PMS.

### 3.6. Proposed major SAM degradation pathway

Fig. 13 presents the main SAM degradation pathways in the NG600/PMS system while the mass spectra of the detected intermediates are presented in Fig. S10. A total of 5 intermediates were detected from the mass spectra. Based on the detected intermediates, the main SAM degradation pathways are proposed. The first reaction step for SAM degradation involves electron transfer reaction between  $\text{SO}_4^{\cdot-}$  and the aromatic amine group of SAM to form nitroso- and nitro- substitutional

SAM (A,  $m/z$  (-) 227.1 and B,  $m/z$  (-) 243.1, respectively) [59,60]. Considering that the amine group is an important bioactive functional group of sulfonamide antibiotics, oxidation of the amine group can effectively remove the bioactivity of SAM [61]. When excessive ROS are present, the S-C bond of B is cleaved, leading to the formation of NB (C,  $m/z$  (-) 122.0). Several SAM byproducts were also detected at  $m/z$  (-) = 138.1 and 305.2, which could be the hydroxylated and polymerized SAM byproducts, respectively. Subsequently, the ring opening reaction takes place and the SAM intermediates are further degraded to mineral acids, inorganic anions, CO<sub>2</sub> and H<sub>2</sub>O. The mineralization of SAM is further evidenced by the results of TOC removal efficiency of 58% (at  $t = 1$  h, [PMS] = 0.5 mM, [SAM] = 10 mg L<sup>-1</sup>, [NG600] = 0.2 g L<sup>-1</sup>, pH = 7).

### 3.7. Reusability

The reusability of NG600 is shown in Fig. 14. Compared with 1st run (100% SAM removal within 50 min), the SAM degradation efficiency decreased to 92% and 58% within 120 min in the 2nd and 3rd



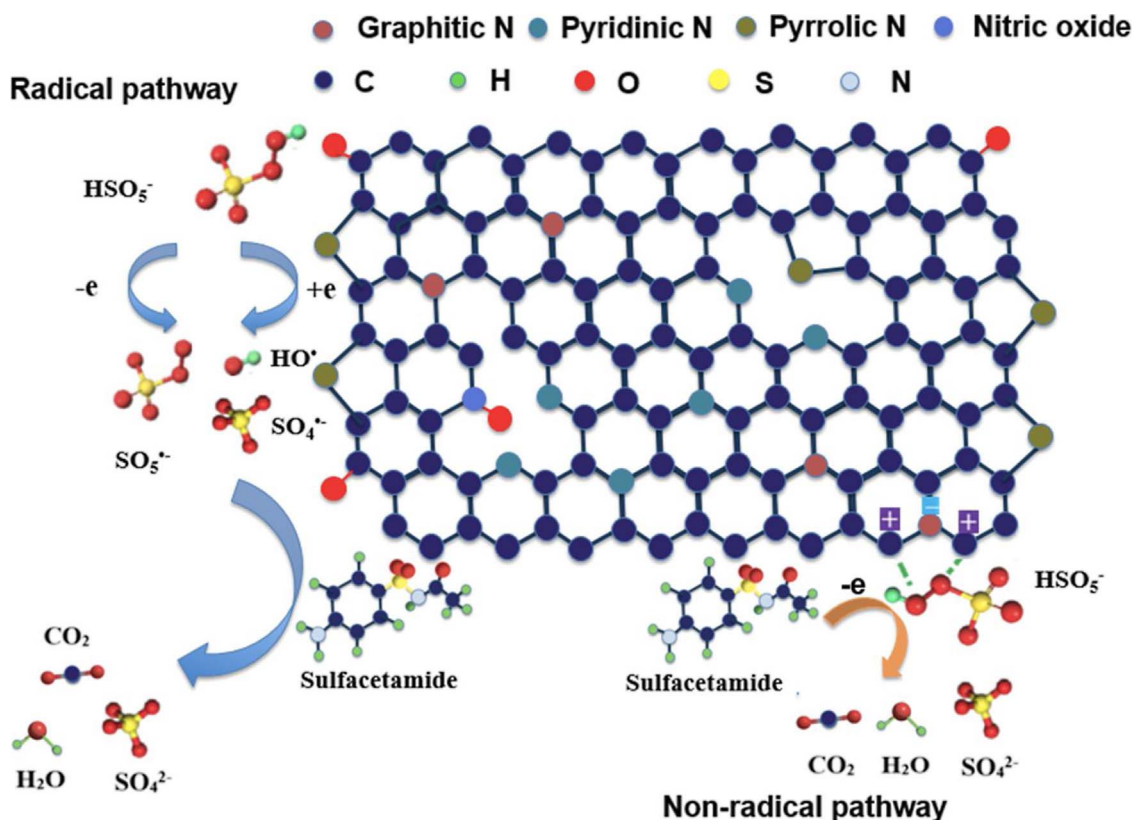


Fig. 11. Mechanism of PMS activation and SAM degradation on NG600.

run, respectively. To gain insights into the reusability of NG600, the N bonding configuration was analyzed by XPS (Fig. S11). As shown in Table 3, the contents of graphitic N (from 25.9%N to 11.9%N), pyridinic N (from 38.4%N to 32.2%N) and nitric oxide (from 3.94%N to 3.34%N) all decreased, whereas pyrrolic N increased from 31.8%N to 52.2%N. Overall, the total N content of the NG600 remained unchanged (5% reduction after 3rd run), indicating that dopant reconstruction occurred in the graphene network during PMS activation process, and graphitic N, pyridinic N and nitric oxide were converted to pyrrolic N (Eq. (8)).



The deactivation of NG600 are mainly due to the occupation of active sites by the SAM intermediates adsorbed and the change in the N

bonding configuration, inhibiting the radical production and outer-sphere interaction. It was reported that in terms of formation energies of the three N types, pyrrolic N and pyridinic N are significantly more stable than graphitic N by about 110 kJ/mol. Pyrrolic N is slightly more stable than the pyridinic N [62]. In an oxidative environment of NG600/PMS system, the reconstruction of N dopants could occur due to the attack of ROS (e.g.  $\text{SO}_4^{\bullet-}$  and  $\text{HO}^{\bullet}$ ) on pyridinic N and graphitic N (cannibalistic reaction), resulting in the conversion of pyridinic N/graphitic N to a more stable pyrrolic N. There are two possible ways to recover the catalytic activity of NG: (1) optimizing the operational conditions to reduce PMS dosage in order to suppress the N bonding configuration conversion; (2) employing the heat treatment for the passivated NG [63], given high thermal annealing temperature favors the formation of graphitic N and can remove the adsorbed

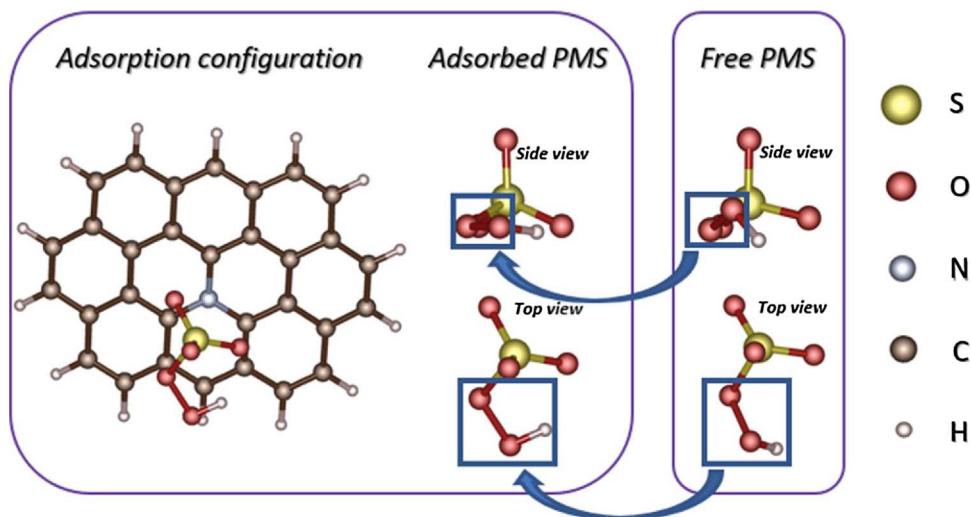


Fig. 12. Structural information of adsorbed and free PMS based on DFT calculation.

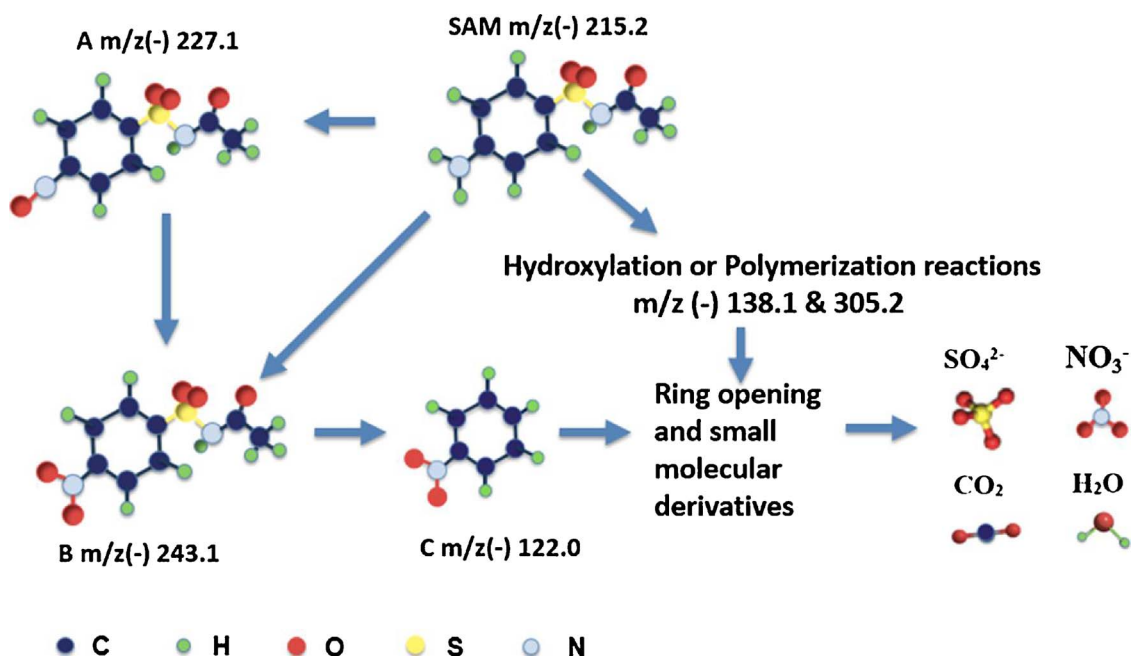


Fig. 13. The main SAM degradation pathways in the NG600/PMS system (Condition: [PMS] = 0.5 mM, [SAM] = 10 mg L<sup>-1</sup>, [catalyst] = 0.2 g L<sup>-1</sup>, pH = 7).

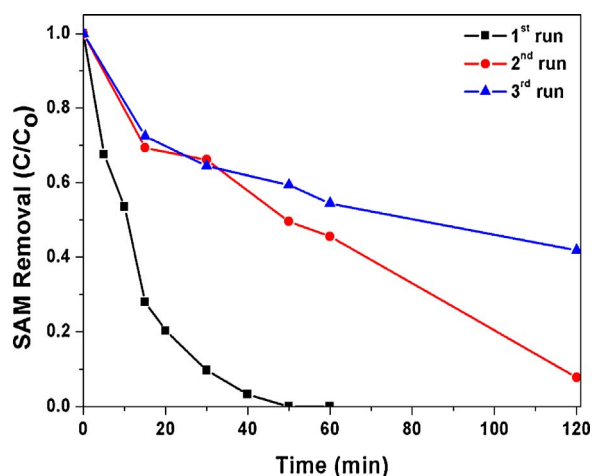


Fig. 14. Reusability of NG600 (Condition: [PMS] = 0.5 mM, [SAM] = 10 mg L<sup>-1</sup>, [catalyst] = 0.2 g L<sup>-1</sup>, pH = 7).

**Table 3**  
Chemical composition of the fresh NG600 and used NG600.

	N	O/C	N/C	Pyridinic N	Pyrrolic N	Graphitic N	Nitric oxide
	wt%	at. %	at. %	N <sub>pyridinic</sub> /N <sub>total</sub> (%)	N <sub>pyrrolic</sub> /N <sub>total</sub> (%)	N <sub>graphitic</sub> /N <sub>total</sub> (%)	N <sub>nitricoxide</sub> /N <sub>total</sub> (%)
NG600	16.0	8.00	18.3	38.4	31.8	25.9	3.94
NG600 3rd run	15.2	10.0	17.6	32.2	52.5	11.9	3.34

Weight percentages of carbon, nitrogen and oxygen were analyzed by CHNS/O analyzer. Atomic percentages of pyridinic N, pyrrolic N, graphitic N, nitric oxide and C=O were analyzed by XPS.

intermediates. Given the relationship between the cannibalistic reaction and N dopants reconstruction is not clear enough, further investigation is needed to probe this relationship and develop more efficient and robust carbocatalysts with certain structures, such as the

core-shell structure with excellent tunability and stability [64] or with some specifically engineered reactive functional groups that can withstand harsh oxidative environment [11].

#### 4. Conclusion

The XPS results demonstrated that four N bonding configurations, namely, pyridinic N, pyrrolic N, graphitic N and nitric oxide, can occur on the doped graphene. Due to their different thermal stabilities and catalytic activities, the contents of different N species and the catalytic performance of NGs can be well controlled by the thermal annealing temperature. The N doping level and the contents of pyridinic N, pyrrolic N and C=O groups of NG400-NG800 manifested a negative correlation with the thermal annealing temperature. The contents of graphitic N and nitric oxide correlated positively with the thermal annealing temperature. The NG endowed with catalytic activity should be synthesized at thermal annealing temperatures of  $\geq 500^\circ\text{C}$ . The NG600 with a higher N doping level (16.0 wt%) and an optimal amount of pyridinic N (38.4%), pyrrolic N (31.8%), graphitic N (25.9%) and C=O groups (43.7%) exhibited the best performance for SAM decomposition via PMS activation. NG600 was superior as a good PMS activator over NGs prepared via other optimized methods found in the literature. Milder synthesis methods or adoption of melamine as a nitrogen source were inefficacious to produce desirable N bonding configurations. The efficiency of SAM degradation followed the order of NG600 > NG-NH<sub>4</sub>NO<sub>3</sub>-air > NG-urea-HT > NG-melamine-N<sub>2</sub>. The SSA contributed less significantly than N doping to the SAM degradation performance. It was operationally more economical to improve the SAM degradation by increasing catalyst loading than PMS dosage in the NG/PMS system. Radical pathway contributed more to SAM degradation than non-radical pathway. SO<sub>4</sub><sup>2-</sup> was the key reactive species for the SAM degradation in the NG/PMS system. The conversion of graphitic N and pyridinic N to pyrrolic N contributed to the deactivation of NG600. Further efforts can be put in improving the stability of carbocatalysts. This study gives a further insight into the role of different surface N functional groups in the PMS activation, facilitating the future development in carbocatalysts engineering via chemical functionalization with the specific reactive groups.

## Appendix A. Supplementary data

Supplementary data associated with this article can be found, in the online version, at <https://doi.org/10.1016/j.apcatb.2017.11.071>.

## References

- [1] J. Chen, P. Sun, X. Zhou, Y. Zhang, C.H. Huang, *Environ. Sci. Technol.* 49 (2015) 4218–4225.
- [2] J. Chen, P. Sun, Y. Zhang, C.H. Huang, *Environ. Sci. Technol.* 50 (2016) 12156–12165.
- [3] C. Walsh, *Antibiotics: Actions, Origins, Resistance*, ASM Press, Washington, D.C, 2003, p. c2003.
- [4] W. Baran, E. Adamek, A. Sobczak, A. Makowski, *Appl. Catal. B: Environ.* 90 (2009) 516–525.
- [5] W.-D. Oh, Z. Dong, G. Ronn, T.-T. Lim, *J. Hazard. Mater.* 325 (2017) 71–81.
- [6] J. Chen, X. Zhou, Y. Zhang, H. Gao, *Sci. Total Environ.* 432 (2012) 269–274.
- [7] C. Adams, Y. Wang, K. Loftin, M. Meyer, *J. Environ. Eng.* 128 (2002) 253–260.
- [8] L.D. Nghiem, A.I. Schäfer, M. Elimelech, *Environ. Sci. Technol.* 39 (2005) 7698–7705.
- [9] P. Westerhoff, Y. Yoon, S. Snyder, E. Wert, *Environ. Sci. Technol.* 39 (2005) 6649–6663.
- [10] F. Ingerslev, B. Halling-Sorensen, *Environ. Toxicol. Chem.* 19 (2000) 2467–2473.
- [11] W.D. Oh, Z. Dong, T.T. Lim, *Appl. Catal. B: Environ.* 194 (2016) 169–201.
- [12] J. Chen, W. Hong, T. Huang, L. Zhang, W. Li, Y. Wang, *Environ. Sci. Pollut. Res.* 23 (2016) 18564–18574.
- [13] J.Y. Pu, J.Q. Wan, Y. Wang, Y.W. Ma, *RSC Adv.* 6 (2016) 91791–91797.
- [14] L.W. Matzek, K.E. Carter, *Chemosphere* 151 (2016) 178–188.
- [15] F. Ghanbari, M. Moradi, *Chem. Eng. J.* 310 (Part 1) (2017) 41–62.
- [16] F. Gong, L. Wang, D. Li, F. Zhou, Y. Yao, W. Lu, S. Huang, W. Chen, *Chem. Eng. J.* 267 (2015) 102–110.
- [17] S. Indrawirawan, H. Sun, X. Duan, S. Wang, *Appl. Catal. B: Environ.* 179 (2015) 352–362.
- [18] R.J. Nicholls, A.T. Murdock, J. Tsang, J. Britton, T.J. Pennycook, A. Koós, P.D. Nellist, N. Grobert, J.R. Yates, *ACS Nano* 7 (2013) 7145–7150.
- [19] H.J. Xiang, B. Huang, Z.Y. Li, S.H. Wei, J.L. Yang, X.G. Gong, *Phys. Rev. X* 2 (2012) 1–7.
- [20] Z. Luo, S. Lim, Z. Tian, J. Shang, L. Lai, B. MacDonald, C. Fu, Z. Shen, T. Yu, J. Lin, *J. Mater. Chem.* 21 (2011) 8038–8044.
- [21] H. Sun, Y. Wang, S. Liu, L. Ge, L. Wang, Z. Zhu, S. Wang, *Chem. Commun.* 49 (2013) 9914–9916.
- [22] C.H. Choi, S.H. Park, S.I. Woo, *ACS Nano* 6 (2012) 7084–7091.
- [23] X. Li, H. Wang, J.T. Robinson, H. Sanchez, G. Diankov, H. Dai, *J. Am. Chem. Soc.* 131 (2009) 15939–15944.
- [24] X. Bai, Y. Shi, J. Guo, L. Gao, K. Wang, Y. Du, T. Ma, *J. Power Sources* 306 (2016) 85–91.
- [25] X. Duan, Z. Ao, H. Sun, S. Indrawirawan, Y. Wang, J. Kang, F. Liang, Z.H. Zhu, S. Wang, *ACS Appl. Mater. Interfaces* 7 (2015) 4169–4178.
- [26] S. Indrawirawan, H. Sun, X. Duan, S. Wang, *J. Mater. Chem. A* 3 (2015) 3432–3440.
- [27] X. Duan, H. Sun, Y. Wang, J. Kang, S. Wang, *ACS Catal.* 5 (2015) 553–559.
- [28] T. Zhang, Y. Chen, Y. Wang, J. Le Roux, Y. Yang, J.P. Croué, *Environ. Sci. Technol.* 48 (2014) 5868–5875.
- [29] D. Li, X. Duan, H. Sun, J. Kang, H. Zhang, M.O. Tade, S. Wang, *Carbon* 115 (2017) 649–658.
- [30] Q. Zhang, A. Jia, Y. Wan, H. Liu, K. Wang, H. Peng, Z. Dong, J. Hu, *Environ. Sci. Technol.* 48 (2014) 14317–14325.
- [31] W.S. Hummers Jr., R.E. Offeman, *J. Am. Chem. Soc.* 80 (1958) 1339.
- [32] J. Tai, J. Hu, Z. Chen, H. Lu, *RSC Adv.* 4 (2014) 61437–61443.
- [33] W.D. Oh, S.K. Lua, Z. Dong, T.T. Lim, *J. Mater. Chem. A* 2 (2014) 15836–15845.
- [34] X. Duan, Z. Ao, H. Sun, S. Indrawirawan, Y. Wang, J. Kang, F. Liang, Z.H. Zhu, S. Wang, *ACS Appl. Mater. Interfaces* 7 (2015) 4169–4178.
- [35] F. Dong, L. Wu, Y. Sun, M. Fu, Z. Wu, S.C. Lee, *J. Mater. Chem.* 21 (2011) 15171–15174.
- [36] X. Duan, H. Sun, Z. Ao, L. Zhou, G. Wang, S. Wang, *Carbon* 107 (2016) 371–378.
- [37] R. Wang, Y. Wang, C. Xu, J. Sun, L. Gao, *RSC Adv.* 3 (2013) 1194–1200.
- [38] S. Stankovich, D.A. Dikin, R.D. Piner, K.A. Kohlhaas, A. Kleinhammes, Y. Jia, Y. Wu, S.T. Nguyen, R.S. Ruoff, *Carbon* 45 (2007) 1558–1565.
- [39] Z. Lin, G. Waller, Y. Liu, M. Liu, C.P. Wong, *Adv. Energy Mater.* 2 (2012) 884–888.
- [40] X.J. Li, X.X. Yu, J.Y. Liu, X.D. Fan, K. Zhang, H.B. Cai, N. Pan, X.P. Wang, *Chin. J. Chem. Phys.* 25 (2012) 325–329.
- [41] S. Park, J. An, J.R. Potts, A. Velamakanni, S. Murali, R.S. Ruoff, *Carbon* 49 (2011) 3019–3023.
- [42] L. Costa, G. Camino, *J. Therm. Anal.* 34 (1988) 423–429.
- [43] S.A. Hasan, E.K. Tsekoura, V. Sternhagen, M. Strömme, *J. Phys. Chem. C* 116 (2012) 6530–6536.
- [44] M. Serebych, D. Hulicova-Jurcakova, G.Q. Lu, T.J. Bandoz, *Carbon* 46 (2008) 1475–1488.
- [45] P.M. Schaber, J. Colson, S. Higgins, D. Thielen, B. Anspach, J. Brauer, *Thermochim. Acta* 424 (2004) 131–142.
- [46] G. Liao, S. Chen, X. Quan, H. Yu, H. Zhao, *J. Mater. Chem.* 22 (2012) 2721–2726.
- [47] S.M. Li, S.Y. Yang, Y.S. Wang, C.H. Lien, H.W. Tien, S.T. Hsiao, W.H. Liao, H.P. Tsai, C.L. Chang, C.C.M. Ma, C.C. Hu, *Carbon* 59 (2013) 418–429.
- [48] W.-D. Oh, S.-K. Lua, Z. Dong, T.-T. Lim, *J. Hazard. Mater.* 284 (2015) 1–9.
- [49] G.P. Anipsitakis, D.D. Dionysiou, M.A. Gonzalez, *Environ. Sci. Technol.* 40 (2006) 1000–1007.
- [50] H.V. Lutze, N. Kerlin, T.C. Schmidt, *Water Res.* 72 (2015) 349–360.
- [51] B. Frank, J. Zhang, R. Blume, R. Schlögl, D.S. Su, *Angew. Chem. – Int. Ed.* 48 (2009) 6913–6917.
- [52] J. Ziajka, W. Pasiuk-Bronikowska, *Atmos. Environ.* 39 (2005) 1431–1438.
- [53] M.E. Lindsey, M.A. Tarr, *Environ. Sci. Technol.* 34 (2000) 444–449.
- [54] G.V. Buxton, C.L. Greenstock, W.P. Helman, A.B. Ross, *J. Phys. Chem. Ref. Data* 17 (1988) 513–886.
- [55] P. Neta, V. Madhavan, H. Zemel, R.W. Fessenden, *J. Am. Chem. Soc.* 99 (1977) 163–164.
- [56] A. Lawrence, C.M. Jones, P. Wardman, M.J. Burkitt, *J. Biol. Chem.* 278 (2003) 29410–29419.
- [57] M. Zalibera, P. Raptá, A. Staško, L. Brindzová, V. Brezová, *Free Radic. Res.* 43 (2009) 457–469.
- [58] M.J. Davies, B.C. Gilbert, J.K. Stell, A.C. Whitwood, *J. Chem. Soc. Perkin Trans. 2* (1992) 333–335.
- [59] Y. Ji, Y. Fan, K. Liu, D. Kong, J. Lu, *Water Res.* 87 (2015) 1–9.
- [60] M. Mahdi Ahmed, S. Barbati, P. Doumenq, S. Chiron, *Chem. Eng. J.* 197 (2012) 440–447.
- [61] W.-D. Oh, V.W. Chang, Z.-T. Hu, R. Goei, T.-T. Lim, *J. Chem. Eng.* 323 (2017) 260–269.
- [62] Z. Tian, S. Dai, D.E. Jiang, *Chem. Mater.* 27 (2015) 5775–5781.
- [63] Y. Guo, Z. Zeng, Y. Zhu, Z. Huang, Y. Cui, J. Yang, *Appl. Catal. B: Environ.* 220 (2018) 635–644.
- [64] J.F. Li, Y.J. Zhang, S.Y. Ding, R. Panneerselvam, Z.Q. Tian, *Chem. Rev.* 117 (2017) 5002–5069.